Ultrasensitive Nanostructured Capacitive Sensors; Fabrication, Auxeticity, Capacitive Sensitivity, and Human-Machine Interface

Zhongjie Qian

A dissertation

submitted in partial fulfillment of the

requirements for the degree of

Doctor of Philosophy

University of Washington

2022

Reading Committee:

Jae-Hyun Chung, Chair

Krithika Manohar

Anthony Dichiara

Program Authorized to Offer Degree:

Mechanical Engineering

University of Washington

Abstract

Ultrasensitive Nanostructured Capacitive Sensors; Fabrication, Auxeticity, Capacitive Sensitivity, and Human-Machine Interface

Zhongjie Qian

Chair of the Supervisory Committee:

Jae-Hyun Chung

Department of Mechanical Engineering

Machine and robots have been widely employed in modern manufacturing, factories, medicares, and our daily lives. Various sensors have been developed for human-robot collaboration (HRC) to offer a customized interface. However, the multiple challenges including high cost, production, sensitivity, and flexibility limit versatile sensor applications to HRC.

In this dissertation, a novel capacitive sensor made of carbon nanotube paper composite (CPC) will be studied and characterized to enable a low-cost, high-performance sensing platform. Based on a wet stretching method, the auxetic behavior of the carbon nanotube composite (CPC) is studied and characterized, which is related to the capacitive sensing performance. Using the fabrication process, the capacitive sensors made of molecular junctions are produced to enable the highly sensitive detection of humidity and liquid level.

Using the co-planar configuration of CPC electrodes, a capacitive sensor is fabricated to monitor humidity change. The sensing mechanism of capacitive response is studied in the context of the molecular junctions among the conductive fibers. Due to auxeticity and buckling, the capacitance forms among the radially diverging structures, which enhances the sensitivity to humidity and moisture.

A highly sensitive capacitive sensor is studied for non-contact liquid level detection by using the single electrode sensor made of fractured CPC. The liquid level is measured by the capacitance value change induced by the dimensional change of the liquid. The detection for both non-conductive and conductive containers is characterized by developing the differential measurement configuration. Simulation and experimental studies are conducted to understand the liquid sensing mechanism. The sensitivity and accuracy in terms of liquid volume and liquid level are characterized by the dimensions.

To validate the use of CPC sensors on human-machine interface, a smart pad is fabricated for gesture recognition. The real-time monitoring model is developed and applied to motion recognition. Artificial intelligence algorithm is used to develop the initial gesture recognition platform. The accuracy of the prediction model is evaluated.

In summary, the dissertation presents the characteristics of the capacitive sensor made of fractured CPC and the applications to humidity and liquid detection. In combination with the sensors, the developed gesture recognition platform can contribute to human-machine interface and human-robot collaboration. For example, monitoring of liquid level will aid the automation and smart control of vending machine, factory production, food processor, etc. The fabricated sensor is cost-effective, flexible, and versatile with a small form factor, which will offer huge potential in the next generation sensing platform that benefits the HRC.

TABLE OF CONTENTS

LIST OF TABLES

LIST OF FIGURES

Chapter 1. INTRODUCTION

The overarching goal of this research is to build a sensing framework for future manufacturing environments. Such a sensing platform can offer versatile manufacturing platforms of Human-Robot Collaboration (HRC) regardless of factory locations and workforce size. Operators or managers working with such platform will be given useful information from translating complex data processed by machines. This allows for unprecedented human-machine collaboration platform, which is invaluable for a major applications of digital manufacturing companies (e.g., 3D printing, CNC) and microfactories. A novel capacitive sensor with human factor-involved artificial intelligence algorithms will be constructed to enable a low cost, highly sensitive smart platform that assures the productivity, and satisfaction of HRC. To this end, nano capacitive sensors in combination with operation and machine learning algorithms will build interactive and safe environment between humans and machines.

1.1 WORK CONTENT

The work context we envision is that the future microfactories will be empowered by a large array of inexpensive nanosensors to support highly cost-effective HRC. The development of microfactories has created novel concepts for unprecedented products by overcoming previous manufacturing challenges. Designing a new technological model of a microfactory will enhance revenues and increase the adaptation of new technologies. Various customized tasks can be conducted in an efficient manner. The sensing technology integrated with system engineering and human-computer interface will empower new

microfactories to be more maneuverable and flexible. Such a change will have a positive impact on our society, where microfactories are gaining momentum as we continue to expand the infrastructure. Furthermore, producing innovative products with an intelligent environment requires a smart facility. HMI is one of the most prominent trends shaping the future manufacturing environment. A well-organized HMI can enhance work performance, resolve more complex tasks, and build a safe ergonomic environment. Such a microfactory will be more agile and swifter to cope with the demands of the community and society. Versatile, competitive nanosensors will play significant roles enhancing productivity and improve human-robot communication.

1.2 FUTURE TECHNOLOGY

In an intelligent, small factory, a small number of various products are manufactured that have a short life cycle. The workers in such a factory will require more frequent updates, continued training on production trends and new information. Various kinds of manufacturing tools need to be introduced, such as, 3D printers, computerized machining tools. The future factory will be armed with the various sensors for interactive communication and will be ergonomic with safe management that ensures privacy and security protection. In addition to camera-based sensor systems, a very large number of non-image-based sensors could be employed to monitor the necessary parameters for interactive communication.

The major roles of the sensors are to provide feedback from the manufacturing process, monitor the factory's operation, and provide an interface for human and machine. In addition, the sensors detecting human motion and the robots' action will offer

customized feedback to either machine or an operator. For example, robots will react to workers according to their working speed, skill, and orders that are captured by sensors. The worker-centered HRC can compensate worker's fatigue in order to maintain product quality and release strain. To meet the requirements, the sensors need to be flexible for use on curved surfaces and inexpensive for massive deployment. The proposed work aims to build a low cost, large array sensor system for an efficient interface between workers and machines.

1.3 Past and Present of Human-Robot Interaction and Collaboration

In the past two hundred years of global industrialization and modernization, humans have experienced three major industrial revolutions. With the start of the 21st century, the fourth industrial revolution began to introduce intelligent robots into medical health, daily life support, and other services. The introduction of intelligent robots has had one of the greatest impacts on the manufacturing field. For example, robotic exoskeletons were developed for the medical rehabilitation of people with disabilities [1]. Hand motor functions were improved for individuals with severe stroke [2]. Robots were introduced to assist surgery to medical doctors [3]. It was reported that the productivity in a food industry was improved by 25% with robotic applications [4]. The population of industrial robots has significantly increased for the last decades due to their contribution to mass production. With the advancement of information technology, robots' performance has evolved from programmed reproducible motion to a more intelligent working partner. The role of robots

has changed from an assistant to a collaborator that can be trained from the actual manufacturing process in real-time.

Instead of pure automation or manual operation, human robot collaboration (HRC) combined the advantages of robots and human operators to offer both the efficiency and the quality of products in both manufacturing and remanufacturing processes. For instance, the bolt assembly lines [5] that required huge quantities and multiple parts were mainly conducted by HRC-based system because of their ability in processing complex operational environments and the reliability of operator's supervision. Also, remanufacturing demanded similar collaboration in the disassembly sequence [6]. A more sophisticated working frame called cyber-physical environment in which human, robot, sensing system and control algorithms are integrated together has been brought up to improve the overall performance of human machine interaction and collaboration [7]. Fig 1.1 gives an example of the working configuration of the HRC for an industrial assembly line of the cyber-physical environment. Workers can instruct the robot with voice and gesture command through audio and video-based sensing system.

Obviously, the development of intelligent robots is a common trend not only in the US but also all over the world. Despite the promising performance of the HRC, confusions still exist in the forms of relationship between human and robot. In some scenarios, the instant reaction to unexpected emergencies continues to be conducted by human workers. Considering the pros and cons of current robotic capability, HRC will be a popular manufacturing platform in modern industry for the next decades.

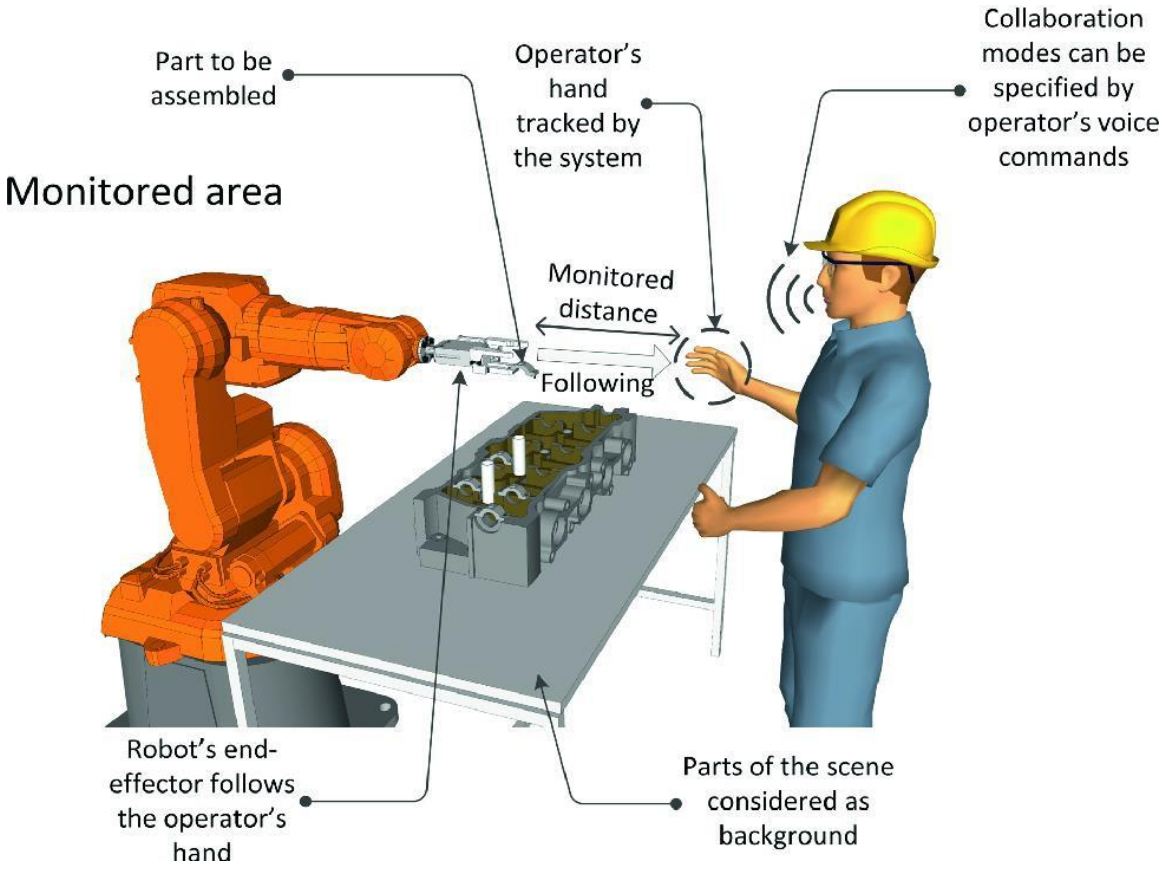

Figure 1.1 Human robot collaboration in assembly

1.4 Role of Sensors in Present HRC

The sensors in an HMI provide communication, environmental and quality control, and safety assurance. For a synergetic HMI, the interactive communication between workers and machines is critical. In HMIs, robots and machines are expected to take orders and learn from human workers. With the training, the assigned tasks need to be completed by robots in collaboration with a worker. An intelligent robot can recognize the instructions from the human supervisor in a form of verbal language, gesture, or body movement. Considering the high ambient noise in manufacturing fields, either gesture or body language is considered for seamless communication. Robots equipped with sensors will

collect and interpret the worker's signals into orders through the mathematical formula of computers. Once all the signals are translated into the instructions that robots can understand, the robots proceed to react according to the commands. Such nonverbal communications can be conducted by image- and nonimage-based sensors [8-11] showing in the Fig 1.2 Literally, robots equipped with cameras or attachable sensors can recognize the complex gesture signal from human workers.

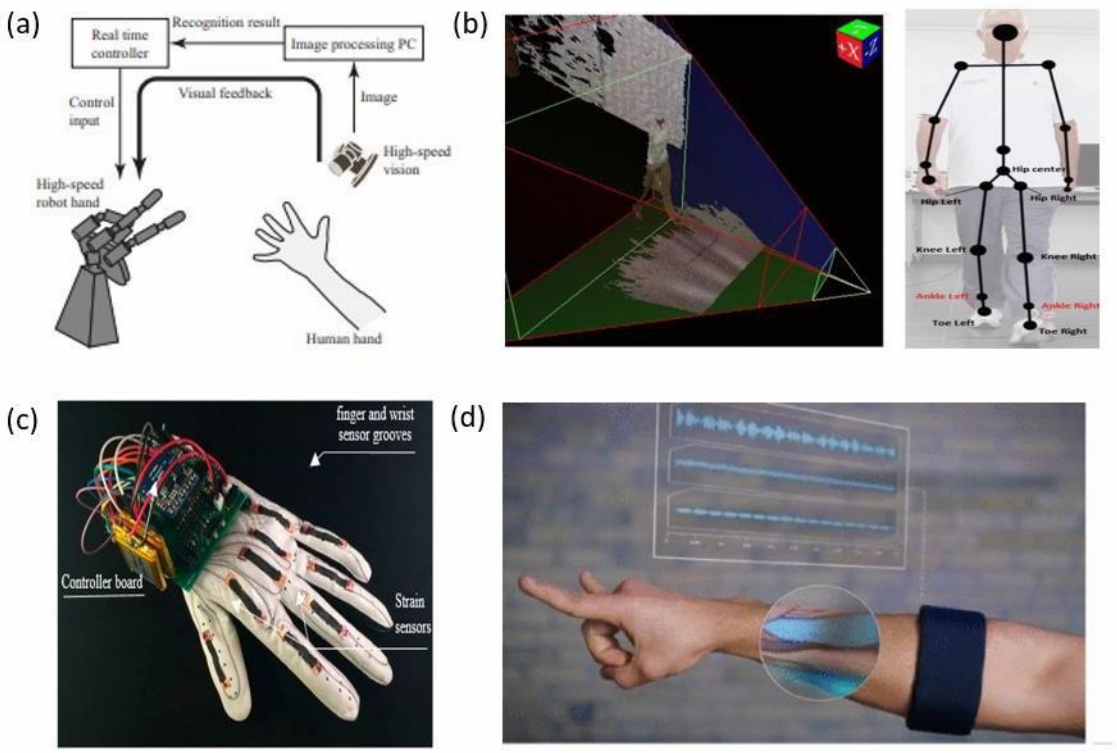

Figure 1.2 (a) single camera-based gesture sensing flow (b)Kinetic device to construct 3D model to detect human motion (c) wearable glove for hand gesture recognition (d) smart band that can sense the motion by detecting the muscle activity

To facilitate the robot's recognition of a worker, inertial sensors have been attached to the worker in the form of wearable sensors. The force sensors help a worker to interact with a robot with manual guidance. The system enhances product quality by increasing the robot's perception with vision systems for robot target identification. Workers with smart wearable devices can have better control through the information provided by the sensor system.

Regarding safety assurance, the current passive form of safety monitoring will not be applicable for safety assurance in the future factory. Since both workers and robots work freely inside the workspace, hardware and software need to be organized for automated control of a factory. An autonomous control system is comprised of various sensors, such as robot safety skin sensor, adaptive vision system, augmented reality glasses, smartwatch interface. As manufacturing factories become more intelligent, a larger number of sensors are required for communication, quality control, and safety assurance.

1.4.1 *Wearable sensors*

The research and application of wearable sensors have been applied for the last few decades in a various fields such as medical [12-14], robotics [15, 16] and entertainment [17]. The types of the well-established wearable sensors can be concluded to strain, pressure, temperature and humidity sensors [18-20]. Basically, those wearable sensors are made of soft material that can be attached to the human skin. The measurements of the sensors are mostly based on mechanical and electrical signals from human activities, which

will be interpreted to healthcare information or interactive data for human machine interface.

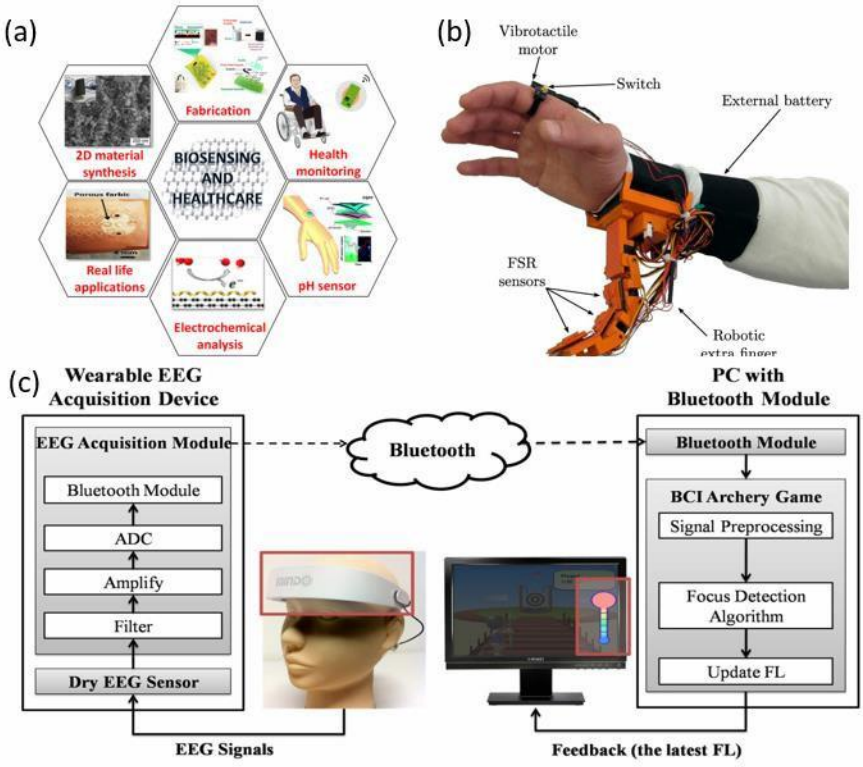

Figure 1.3 Wearable sensors in multiple fields (a) Flexible electrochemical biosensors for clinical analysis (b) The robot extra finger controlled by a vibrating motor (c) Wearable EEG-based device and its application to gaming control

The two important features of current wearable sensors are flexibility and light weight. Humans can wear those sensors without abnormal behaviors. Typically, in healthcare applications, the wearable sensors can be used to monitor human's medical information, such as heart rate, muscle activity to body temperature, humidity [21-23]. Similar to healthcare applications, the temperature and humidity wearable sensors can be applied to monitor the sweating condition of athletes in training and match [24].

The traditional medical information requires in-patient facilities for people to obtain the essential medical diagnosis. With the advent of wearable sensors, medical doctors can help patients with basic healthcare issues through the information given by light and flexible sensors. Although the current wearable sensors do not show accuracy and details in comparison to a FDA approved medical instruments, the accessibility and flexibility of wearable sensors give the potential for home-diagnosis of patients [25]. Another advantage of wearable sensors is the low manufacturing cost, which is affordable to a wider range of users [20].

The wearable sensors also have huge potential in chronic disease diagnosis. Traditional medical instruments are accompanied with heavy weight and constraints. The patients with chronic health issues require daily monitoring without interfering their normal lives [26]. One of the common symptom of the chronic disease is inactivity [27] such as freezing and falling. Sensitive wearable sensors can collect and store the data from the daily movements of patients for further translation to doctors. Based on the collected data, the health condition can be determined. Early diagnosis is crucial for various diseases, such as Parkinson's disease [28].

Besides monitoring body conditions, the smart sensors will be massively used in the human machine interaction and collaboration as discussed previously. Recently, the research interest for wearable sensors has been highly increased because of the enhancement of interaction between human and device. Sensors are embedded with equipment which can be instructed from receiving signals of operators. Various attempts of human machine interface have been conducted in the fields of gesture recognition [29]

and real-time eye tracking [30]. To fulfill the goal of the effective interaction between human and equipment, people have tried multiple types of wearable sensors.

For instance, eye tracking is a prevalent topic in recent years for wearable sensors, since it has a huge potential in healthcare and entertainment. Basic information on neurological disorders and cognitive functions can be obtained by tracking their eye movement through wearable eye trackers. Video game manufacturers can produce the virtual reality (VR) controller with the embedded eye tackers to give the players more immersive and real game experience. Therefore, researchers have put their effort in several kinds of sensors which can effectively provide the interactive platform for users from sensing the users' eye movement. One of the popular sensors is an electrical device that can capture the signal of electro-oculography (EOG) [31], which is altered when the gaze start to move. Another type of sensors is a camera-based device [32, 33], which are also effective in capturing the gaze movement. Eye tracking information can be employed in both real-time and recorded applications for communication.

1.4.2 *Sensors for robotics in industry*

As the technology in chip manufacturing and artificial intelligence is growing exponentially, the robots in the modern factories are not only required to produce the repetitive and tedious job, but also have the ability to process more complex work procedure and collaborate with human workers. To establish the communication between human and robot, the interface or channel is built through a various sensory system. For instance, a force sensor attached on robot can detect the interaction between worker and

robot [34], and the visual feedback through cameras planted on the robots [35]. Both force and impedance sensors can be hybridized with machine learning algorithms [36].

When an effective interaction is well established, robots can not only work for routine industrial use but also handle more sophisticated job like a human worker. Besides intimating a human behavior, the next generation of the robot is capable of receiving instructions from an operator through either video and audio information [37, 38] or gesture recognition based on wearable devices [39, 40]. The enormous amount of research in the area proves that the trend of developing smart robots through a highly effective and efficient communication between human and robots is obvious and promising. Therefore, a sensor system is the foundation of this human-machine interaction, which is the key element for next generation manufacturing.

1.5 CHALLENGES

To accomplish highly efficient communication between humans and machines, the building block is sensing technology. However, various sensing mechanisms and operation algorithms require expertise. Furthermore, there exists a huge disparity in terms of building cost of a different sensing system. It is our fundamental question: can we build a system with the sensor that possesses the features of low cost, high sensitivity, flexibility, large scale manufacturing, and multipurpose?

Current sensors can be classified into two major types. One is contact or wearable sensors that are usually attached to either the surface of human and robot or wearable devices. The other one is a non-contact sensor that can receive either environmental

information like temperature and humidity or visual and audio information such as camera and microphone.

One of the challenges is to maintain accuracy while increasing sensitivity. When the alteration is made to enhance sensitivity, the noise will increase accordingly. Under such circumstances, the sensor may make errors in verifying the signal under action in coupling with environmental noises. Another critical issue of the current wearable sensors is that a sensing capability is restrained in a certain domain. For example, a smart watch now is very popular in healthcare and energy consuming applications such as measuring heart rate, step number, and noise level in surrounding environment. However, the accuracy of the daily activity based on step number and heart rate is not very high because the different levels of working cannot be just reflected by step counts and heart rate [41]. In order to precisely monitor the intensity of the activity, multiple wearable devices should be used to equip a worker who needs to have a full picture of a day.

As for the human robot collaboration in the industrial manufacturing, current sensors do not meet the requirements for an HRC environment in terms of performance, cost, safety and comfort. One of the major concerns of HRC is safe and secure operation. In order to mitigate the risks during manufacturing, the potential hazards need to be addressed to avoid severe accidents or production delays associated with HRC [42]. In the past, automated robots were used to produce repeated and tedious tasks that were pre-programmed without any further instruction. With the diverse demands of products, human operators were involved into the manufacturing line to distribute flexible goals and tasks for robots. The most common way to reduce the risk was to set up a physical fence that basically separated

workers from robots. The method was too conservative to produce HRC synergy by restricting the workspace.

A sensing system was proposed to protect workers from potential injury but also minimize the safety concerns through visible warning and strategically located sensors [42]. As for image-based systems, cameras were used to detect whether the robot motion would physically contact human workers. The advantage of the camera-based sensor was a non-intrusive and relatively easy installation. However, the detection region was restricted by the camera location. The cameras were prone to occlusion and highly dependent on lighting conditions [43]. Moreover, workers felt uncomfortable under the continuous surveillance of cameras. The exposure of recorded images to external information technology was another security concern of a camera system. The use of multiple camera-based sensors could significantly increase the computational and equipment cost. Non-image-based sensors were like the wearable wrist band, jacket [43], and electromyography motor intention prediction technology [44]. Free from lighting restrictions, the wearer's mobility was restricted, which was not favored by workers in the production line. Also, the wearers need to be trained to use sensor technology. The wire harness and additional power sources rendered the wearers uncomfortable in the manufacturing field. For example, gloves and wrist bands with sensors required extra cables, which might not be favored by workers.

Therefore, a new sensing system with the advantages of low-cost, large-scale fabrication, high sensitivity, and versatility is critical to meet all the requirements for future

1.6 OBJECTIVES

To accomplish a framework for a productive, safe, and ergonomic HRC, we envision the construction of a large array of smart, low-cost sensors. An array of nano-sensors is employed to monitor operator's moving pattern and action, which is then interpreted into an order for the robots to conduct an assigned task. We hypothesize that the array of capacitive nanosensors can be produced at low cost, large scale, and work for human-machine interface.

To test the hypothesis, the specific objectives in this dissertation are:

(1) To investigate the auxetic behavior of carbon nanotube paper composites in order to produce a highly sensitive capacitive sensor.

(2) To investigate the humidity sensing mechanism of a CPC nanosensor and to apply the sensors to sweat sensing.

(3) To Investigate the characteristics of single electrode capacitive sensor to measure the liquid level with high sensitivity and large dynamic range.

(4) To characterize differential measurement configuration to improve the resolution and accuracy of capacitive liquid sensing.

To this end, the proposed research outcomes will be a steppingstone for digital manufacturing and automation by offering a highly sensitive and economic sensing solution. Such sensing capability needs to be further developed for human-robot collaboration.

Chapter 2. AUXETICITY AND CAPACITIVE SENSING

2.1 INTRODUCTION OF NOVEL NANOSENSORS

In order to address the challenges in human-machine interface, the novel nanosensors are made of carbon nanotube paper composite (CPC) has been found as the potential material to offer the sensing foundation. Lots of previous research on the paper-based carbon nanotube composites have been proposed and studied because of the fantastic mechanical, thermal, and electrical properties of CNTs [45-47]. Due to the great performance of the composite, the potential applications have been researched as well [48]. are focused on the characterization of CNT-polymer composite [49], however, how to deliver and developing the high performance material mechanically and electrically is the major concern of the most of the studies which remains the interface between CNTs and fibers veiled. In order to figure out the situation in which a multifunctional, highly sensitive sensor can be produced in a low cost and large scale, the first priority is to find out the mechanical and electrical sensing mechanisms.

The paper based composite has been demonstrated as potential sensor in biological and chemical fields [50] due to its large surface area which can be modified as a probe to detecting the target object. Illuminated by the special feature of the high aspect ratio and large surface area, we proposed to create this structure from the CPC sample by stretching through which the specimen will perform auxetic behavior. The auxeticity of the paper material can generate the many high aspect ratio individual fibers from the original thin piece of paper. And we believe that those disconnected cellulose fibers coated with CNTs is the ideal candidate for the capacitive sensing.

2.2 BACKGROUND OF AUXETICITY AND CPC

Auxeticity is a structural property showing negative Poisson's ratio. Most materials in nature demonstrate positive Poisson's ratio showing the shrinkage when a material is stretched. However, the auxetic material with negative Poisson's ratio presents expansion under uniaxial tensile force [51]. Auxetic structures such as chiral structure, re-entrant structure, rotating rigid structure [52-54], could be designed for applications to micro devices [55], medical device [56], aerospace [57], and sensors [58, 59]. Other than designed structures, negative Poisson's ratio were frequently observed in fibrous materials [60]. Paper [61] and non-woven fabrics [62] were discovered to possess auxetic behavior. Periodic, repeating structures [63, 64] could be designed to amplify an auxetic effect. One of the auxetic mechanisms in anisotropic paper consisted of the buckling of out-of-plane fibers under a stretched random matrix. Due to buckling, a large negative Poisson's ratio has been observed for individual fibers [65]. The extreme auxeticity enabled the manipulation of out-of-plane electrical junctions for resistance change. While conventional sensors made of a positive Poisson's ratio showed a resistance increase upon pressure, the resistance of an auxetic material decreases due to the recovery of electrical connections [66, 67].

The carbon nanotube paper composite (CPC) is one of the discovered auxetic materials. In these composites, CNTs deliver electrical conductivity, while cellulose fibers offer the structural frame [68]. Since cellulose fibers are the structural component of a composite, the deformation of cellulose fibers contributes to the auxetic behavior under stretching. In our previous research, the auxetic behavior of CPC has been characterized for elastic and plastic regions [69]. To better control the fracture process, water was printed through a

capillary nozzle to initiate the dissociation of cellulose fibers. CPC could be cracked and fractured at a water-printed region. The auxeticity of the water-printed CPC was pronounced due to the stress concentration of varying elasticity and Poisson's ratio in the dry-wet-dry CPC regions. The uniformly cracked and fractured CPC showed a remarkable resistive sensitivity due to the rapid percolation change under pressure.

2.3 FABRICATION OF THE CAPACITIVE SENSOR

Fig. 2.1(a) shows the fabrication steps for a capacitive sensor made of carbon nanotube-paper composites (CPC) [70]. Similar CNT polymer composite was fabricated and studied [17]. However, different from fabrication process of the previous composite, our CPC sensor was made using wetting and tension. A water line was printed on the middle of the CPC sample in the direction perpendicular to stretching. The stretching causes the fracture at the water-printed region, resulting in a capacitive sensor composed of numerous fibers. The fractured composite was infiltrated with polyurethane for sensing applications.

Fig. 2.1(b) shows the auxetic behavior of a CPC composite under tension. Under stretching, a specimen is compressed along the water-printed region (green arrow), where the buckled matrix expands out-of-plane direction (red arrow). The auxetic behavior organized fibers along the stretching direction and out-of-plane direction. The stress concentration due to different Young's moduli and Poisson's ratios was the main factor for the large auxeticity. The large property difference of the wet and dry regions caused the stress concentration to increase the auxetic behavior, and the stress concentration resulted in the necking of the wet region and the subsequent larger buckling of the cellulose fibers.

In particular, the fractured fibers formed high-aspect-ratio structures producing a high electric field to significantly enhance the capacitive sensitivity.

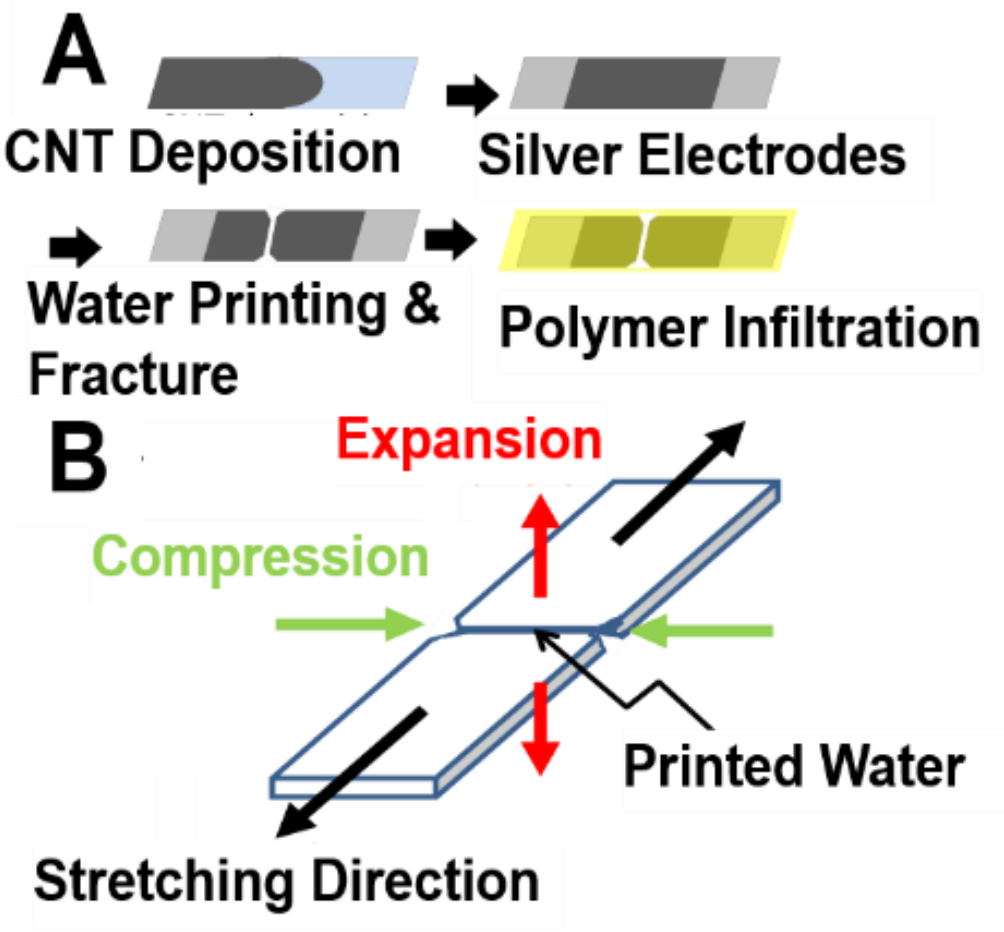

Figure 2.1 (a) Fabrication steps for the capacitive sensor. (b) Illustration of auxetic behavior.

2.4 EXPERIMENT SETUP FOR FABRICATION

CPC preparation: CNT-cellulose composite papers were prepared following a modified TAPPI T-205 standard method [71]. In short, hydroxyl-functionalized multiwalled carbon nanotubes (MWCNTs) were dispersed in a binary mixture of alkali lignin (AL, 99%) and sodium dodecyl sulfate (SDS; 90:10 wt) [72]. Aqueous dispersion of CPAM were first added to pulp fiber solutions (0.3% consistency) and combined on a hot plate at 50°C for 30 minutes. The as-dispersed CNT-OH solutions were then added to the pulp mixture. The combined CNT-OH and pulp suspensions were then filtered, pressed, and dried to form hand sheets. The CNT concentration in CPC was 10 wt %.

Fabrication of CPC capacitive sensors by water-printing and stretching: CPC capacitive sensors were fabricated by controlled water-printing and axial stretching (Fig 2.1) [69]. A 100 μm-thick CPC strip was trimmed to make a 20 mm-long strip. The strip widths of 1, 3, 5, 7, and 10 mm were prepared. Silver paste (MG Chemicals, USA) was applied to both ends of a CPC strip and cured at 70 °C on a hot plate to make electrodes. Using a 0.7 mm-diameter capillary pen, water was printed along the center line without physical contact to CPC.

To produce auxetic behavior, a tensile testing stage was constructed with a uniaxial actuator. The tension was applied with a constant speed of 38 μm/s. To study the auxetic effect of CPC to humidity, humid air was continuously supplied to a CPC specimen through a 12 mm-diameter nozzle in a tensile test. Force and resistance were measured by a load cell (DYMH-103, CALT, China) and a high impedance multimeter (Fluke Corp., USA), respectively. The stress was calculated by $\sigma = \frac{F}{do \times th}$, where F was the force measured by

the load cell, d0 was the initial width of a specimen, and th was the initial thickness (i.e., 100 μm) of the specimen. The axial strain was $\varepsilon = \frac{l-l_0}{l_0}$. CPC specimens without water-printing were also tested to compare auxeticity and capacitive change with water printing.

Auxetic behavior characterization: To investigate the width effect on auxeticity, the specimen widths of 1, 3, 5, 7, and 10 mm were prepared. The auxetic behavior was studied by measuring the thickness changes. In the testing stage (Fig 2.2), a microscope was focused on the water-printed region of the specimen from the top- and side views (x-y and x-z planes). The thickness change of a specimen in water-printing and stretching was measured. The effective Poisson's ratio was computed at the maximum thickness by the following equation:

$$\nu_{eff} = -\frac{(z_{max} - z_0)/z_0}{(l_{max} - l_0)/l_0} \quad (2.1)$$

where Z_{max} and l_{max} denoted the maximum thickness and the length at the thickness, and z0 and l0 denoted the original specimen length and thickness. For both specimens with and without the water-printing, ν_{eff} was computed at strain ranging from 0~0.36. The ν_{eff} of non-water printed paper and CPCs were computed at the fracture strains.

Characterization of fractured CPC: Scanning electron microscopy (SEM, XL830, FEI Company, Hillsboro, OR, USA) was used to study the in-plane and cross-section morphology of water-printed CPC stretched at various strain levels. To ascertain the fracture length and morphology, the CPC was mounted to a flat aluminum stage using double-sided carbon tape and imaged using a 5 kV accelerating voltage with a 5 mm working distance.

2.5 RESULT AND DISCUSSION

Since the stretching induced fracture, the original closely connected fiber network is destructed, the sensor now can be used as a capacitive sensor which gives the sensor the ability to detect the contact and non-contact displacement of both conductive and non-conductive object.

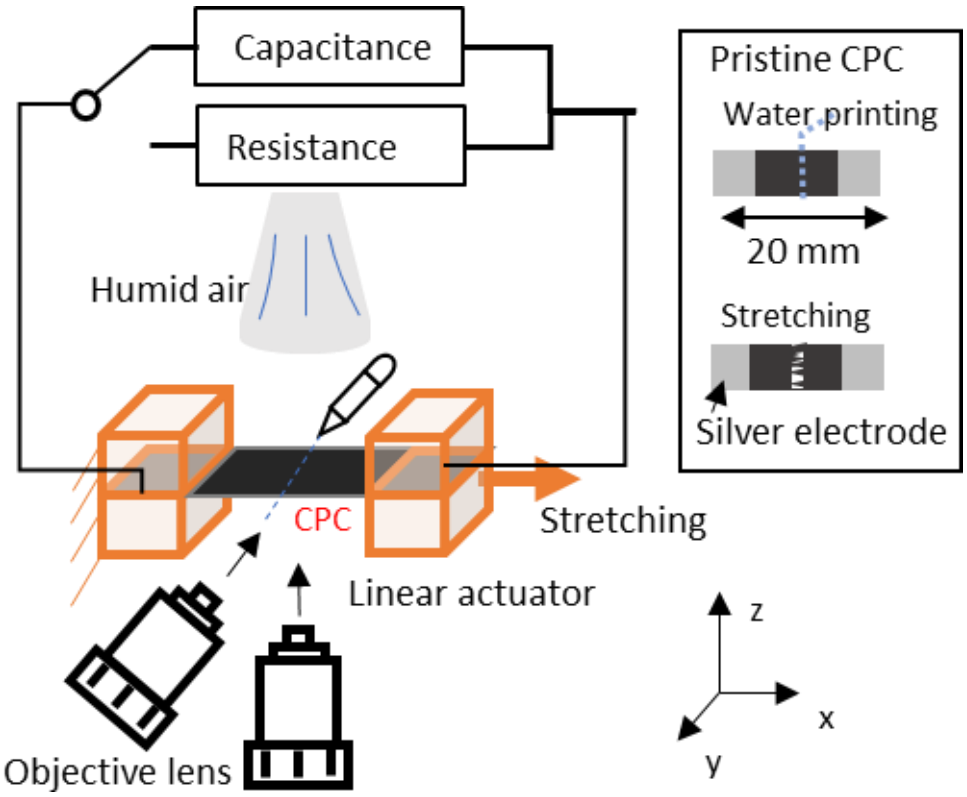

Figure 2.2Test setup to investigate the auxetic behavior through wet stretching method

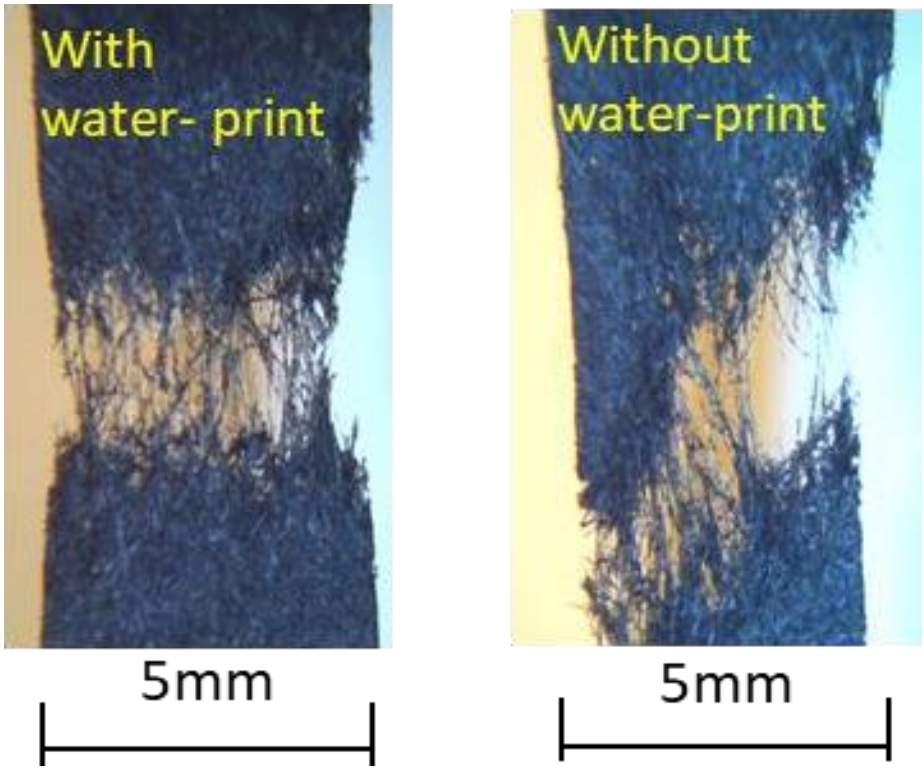

Figure 2.3 Fractured CPC with and without water printing.

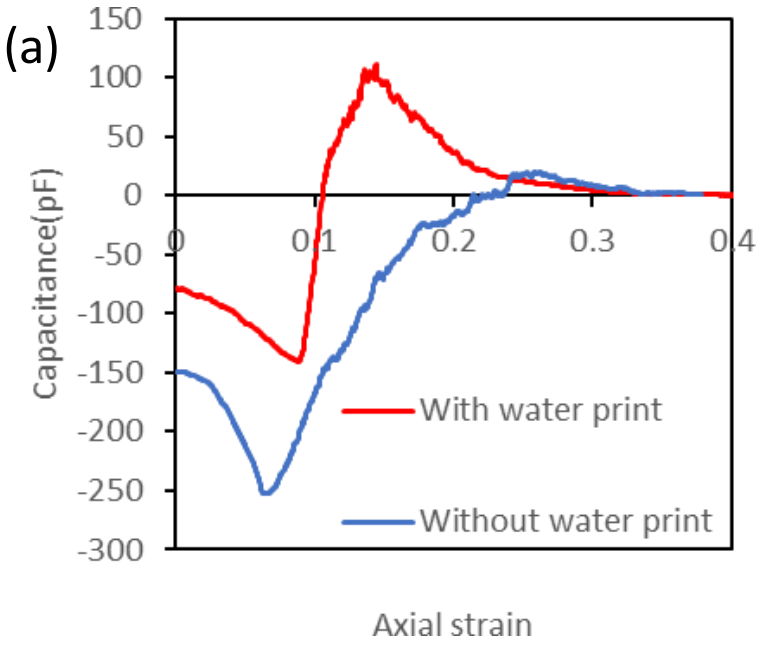

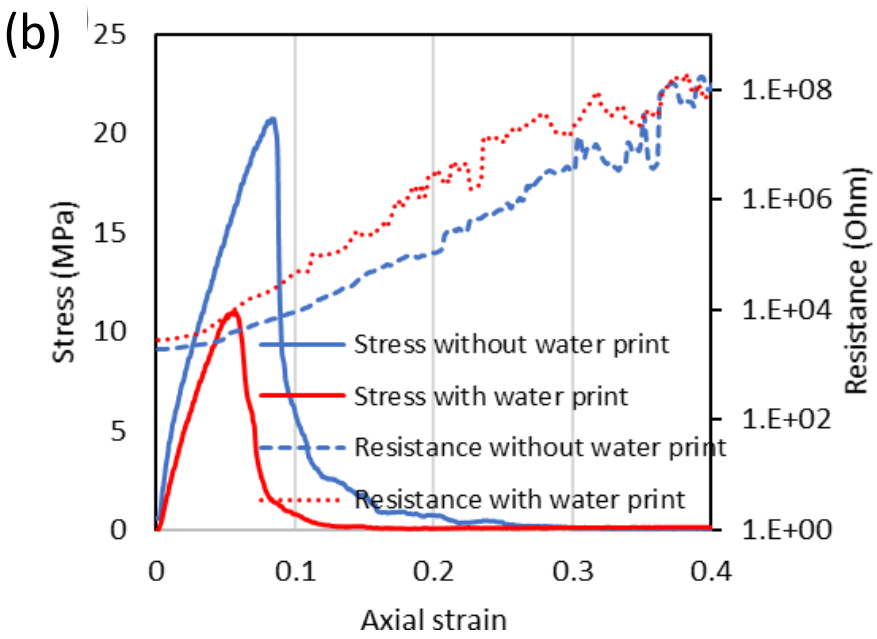

Figure 2.4 (a) Stress-strain relationship for CPC with and without water printing. Resistance change is described on the second y-axis. (b) Capacitance change for CPC with and without water printing.

In the crack, numerous cellulose fibers coated with MWCNTs protrude along the stretching direction. When an external electric potential is applied between two electrodes for capacitance measurement, the electric field increases significantly at the nanotube tips because the length-to-diameter ratio is large. The cantilevered electrodes form a large fringing capacitance, which interacts with robots, workers, and the environment in contact and non-contact modes. The negative Poisson's ratio means that the cantilever fibers bulge in the out-of-plane direction due to the compression and buckling in the width direction. The electrical connection is terminated at this stage, but the fibers are visually connected.

Capacitive and resistive characterization of CPC sensors by water-printing and stretching The CPC sensors were fractured under a water-printed condition using the setup (Fig 2.2). To study the capacitive and resistive changes in coupling with the auxeticity, three CPC sensors were stretched with and without water printing. Optical microscopes were placed to observe the top- and side views of the fracture process. From the top-view images, the CPC samples without and with water printing were clearly differentiated. The crack of the water-printed sensor was created along the water line, perpendicular to the stretching direction. The crack of the CPC without water printing was propagated at a 45-degree angle to the stretching direction due to shear failure (Fig 2.3). Fig 2.4(a) shows the stress-strain relationship for CPC with and without water printing. The strength for a water printed CPC was lower than that of CPC without water printing. The resistance increased by a power law due to rapid increase of percolation.

The capacitive response of the CPC sensors with and without water printing was measured under an RH-100% condition shown in Fig 2.4(b). The nozzle connected to a humidifier was applied directly on the specimen surface in stretching. The capacitance of

the specimens with and without water printing started with negative values because the produced capacitance was in parallel with the electrical resistance. The negative capacitance means the leakage of electric current through resistive connection of CPC. As a CPC specimen started to fracture, the negative capacitance magnitude increased. Note that the dip in the negative capacitance was the characteristic of a capacitance meter circuit not the characteristic of a CPC specimen. According to our characterization of the capacitance meter, as the resistance increased, the negative capacitance magnitude showed a dip followed by the decrease to 0 pF. As the strain crossed 0.1, the capacitance of water-printed CPC became positive while the CPC without water-printing stayed at a negative value at 0.1-strain. Interestingly, the CPC with water-printing reached the maximum capacitive value of 103.3 pF and converged to zero as the distance between two fractured CPC electrodes increased. The two capacitance curves met at 0.24-strain where the samples were completely terminated electrically and mechanically.

Fig. 2.5(a) and 2.5(b) show the SEM images of the cross-section for 5 mm-wide specimens at 0.12 and 0.18 strains, respectively. In comparison to the thickness of the specimen without water-printing, the thickness increase of a water-printed specimen was greater (Fig. 2.6). The thickness increase of a water-printed specimen reached the maximum value when the applied strain was 0.24. As the specimen was completely fractured, the thickness increase stopped with the complete release of a tensional force.

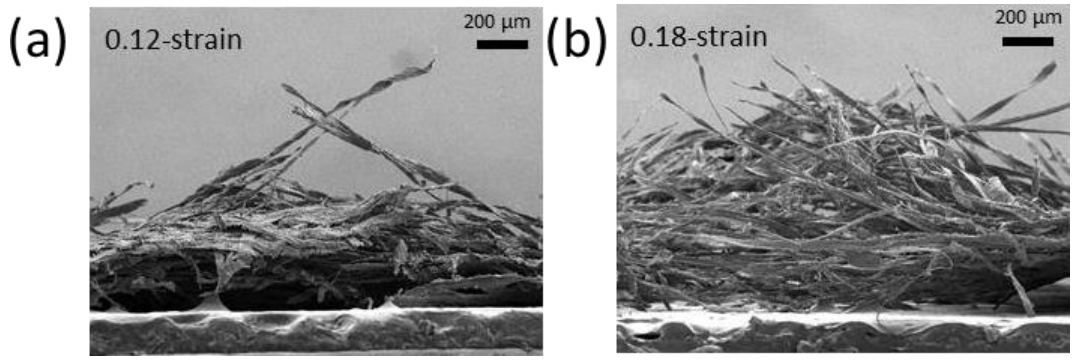

Figure 2.5 (a) and (b) SEM images of the cross section of 5 mm-wide CPC specimens at different strain levels.

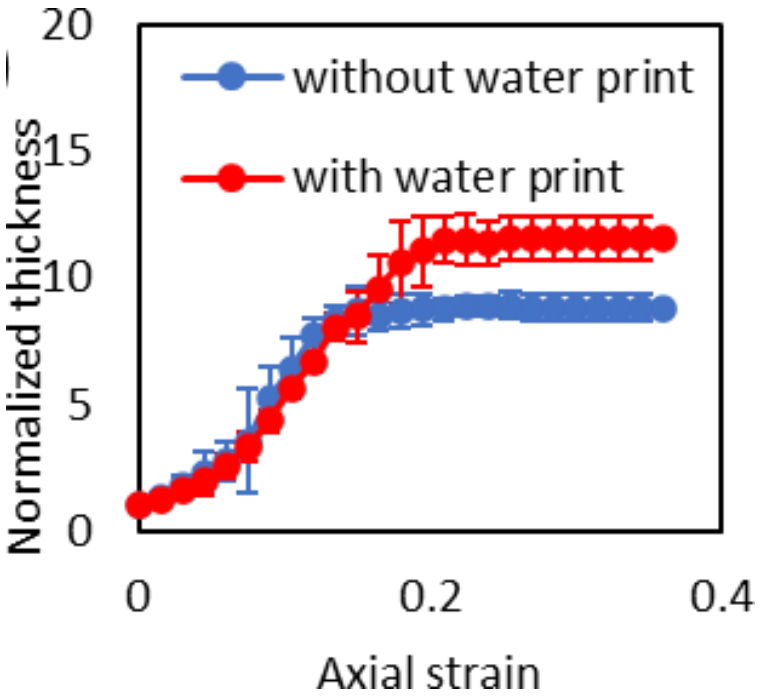

Figure 2.6 Normalized thickness changes according to axial strain for 5-mm wide CPC specimens with and without water printing.

The width increase of water-printed specimens enhanced the auxeticity, which increased the magnitude of Poisson's ratio (Fig 2.7(a)). When the width increased from 1

to 10 mm, the capacitance increase was proportional to the widths between 3 and 10 mm after applying the same 0.24 axial strain (Fig. 2.7(b)). Since the specimen was stretched under RH-100 %, the relationship between sample widths and capacitances demonstrated the sensitivity to humidity. In the graph, a 1 mm-specimen showed the smaller capacitance value than the linear equation given in Fig. 2e. The smaller capacitance at a 1 mm-specimen resulted from the smaller Poisson's ratio as shown in Fig 6d. In comparison to the capacitance made of a trimmed aluminum film having widths between 1 and 10 mm, the CPC capacitance was 41.2 times (Supplementary Information, Fig S1). The fibrous junctions produced by auxeticity evidently increased the capacitance.

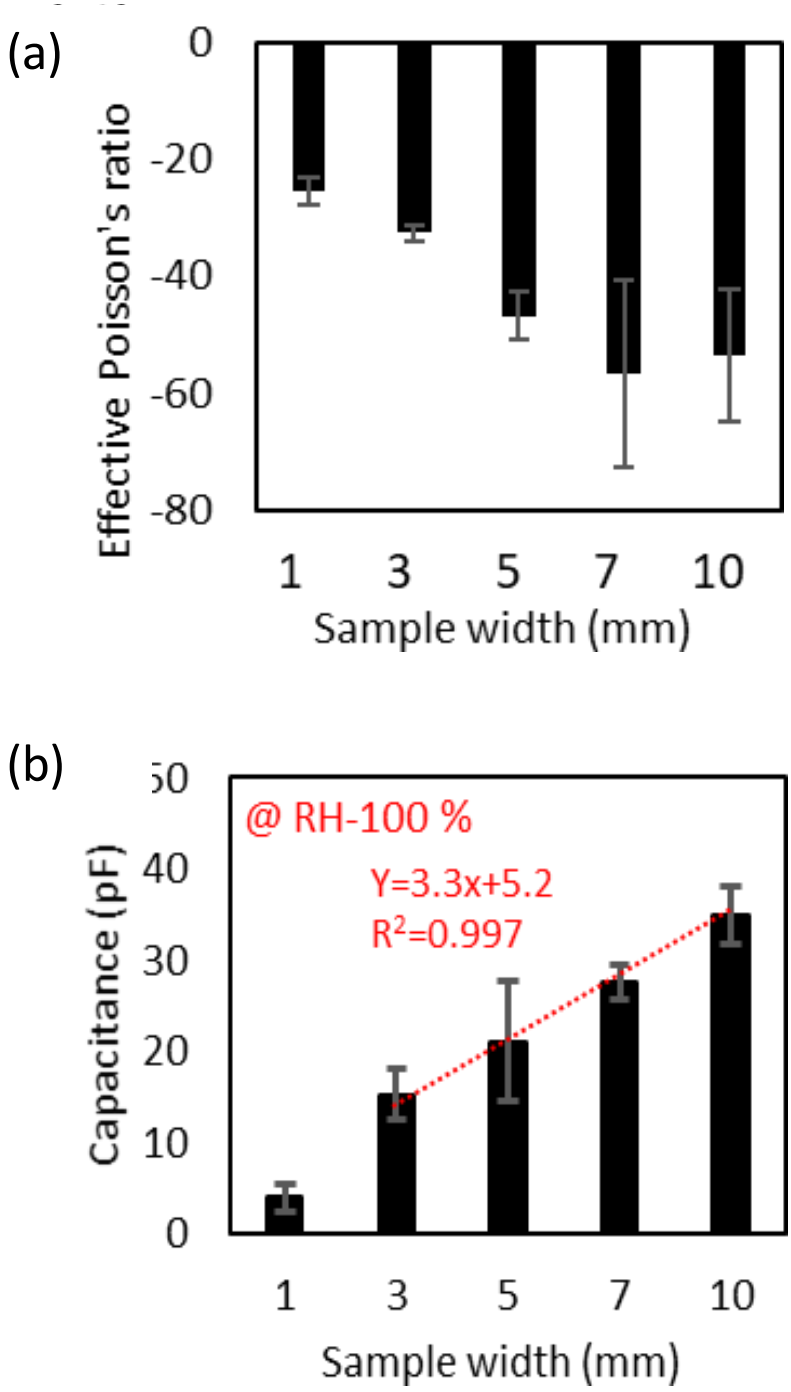

Figure 2.7 (a) Effective Poisson's ratio according to specimen widths (N=3) (b) Capacitance values at strain 0.24 according to specimen widths (N=3).

Fig 2.8 shows the comparison between Poisson's ratio and capacitance. At the smaller widths of a specimen, the capacitance increased as the Poisson's ratio increased. Since the Poisson's ratio saturated for the specimen wider than 3 mm, the capacitance increase was only dependent on the width increase.

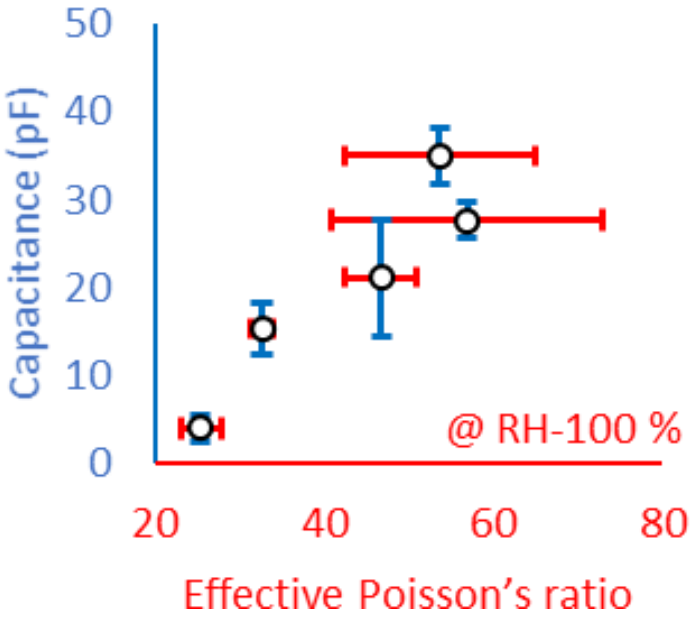

Figure 2.8 Comparison of effective Poisson's ratio and capacitance.

2.6 SIMULATION OF THE CAPACITIVE SENSOR

To analyze the reason of the auxeticity increase due to the width, numerical simulation was conducted using COMSOL Multiphysics. A 1-mm displacement was applied on the right end at the longitudinal direction to simulate the tensile deformation. Because of the positive x-y Poisson's ratio, a compressive stress was generated at the wet region across the central line along the y direction (Fig. 2.9(a), (b), and (c)).

The averaged compressive stress is then compared with the stress from the critical buckling force under the pin-joint conditions, which was calculated as:

$$P_{cr} = \frac{\pi^2 EI}{L^2} \tag{2.2}$$

where the moment of inertia is evaluated across x-axis and L is the width of a CPC strip. A critical buckling stress was obtained by multiplying the cross-sectional area (thickness × width) to the critical buckling force. According to the numerical results (Fig. 2.9(d)), the compression stress could cause buckling of a specimen wider than 1.9 mm. Over the critical width, the CPC specimen could buckle due to the increased aspect ratio (width/thickness = 19). The buckling increased the Poisson's ratio and auxeticity. The numerical results agreed with the experimental results. When the width was greater than 3 mm, the CPC specimen could be buckled with a periodicity, which could reduce the thickness increase. As a result, the capacitance increase was proportional to the width for the specimens wider than 3 mm.

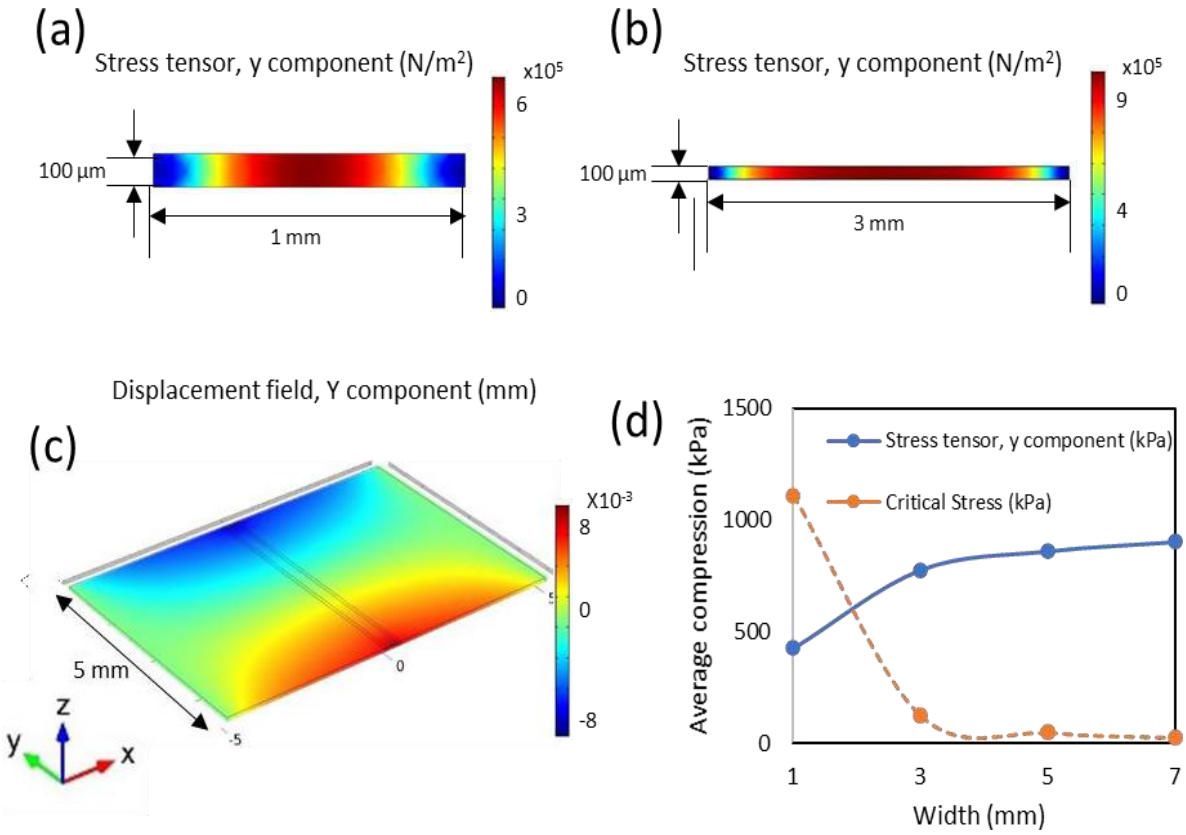

Figure 2.9 (a) Stress distribution on a 1 mm wide-CPC specimen (b) Stress distribution on a 3 mm-wide specimen. (c) Compressive stress built across the width of a 5 mm-wide specimen. (d) Comparison of average compressive stresses and critical buckling stresses according to specimen widths.

Chapter 3. CAPACITIVE SENSORS IN HUMIDITY SENSING

3.1 BACKGROUND

In the CPC sensor, CNTs offer electrical conductivity while cellulose fibers offer the structural frame. Since cellulose fibers are the structural component of a composite, the deformation of cellulose fibers contributes to the auxetic behavior under stretching. In our previous research, the auxetic behavior of CPC has been characterized for elastic and plastic regions

To our knowledge, the capacitive sensing characteristics of an auxetic material has not been studied. The major question is about how the auxetically modified CPC can change capacitive junctions. A designed auxetic structure has been studied to enhance the capacitive strain sensitivity [59]. The capacitive sensitivity of fractured CPC to humidity is yet to be discovered. We hypothesize that water molecules introduced to the conductive fibrous junctions can modify capacitive characteristics in conjunction with auxeticity. To test the hypothesis, this study investigates the capacitive sensitivity to water vapors for various widths of CPC fractured by a wet-stretching method. The capacitive response to humidity is investigated in terms of strain, Poisson's ratio, and CPC widths. As a practical application, humidity and sweat sensing capability is demonstrated.

3.2 EXPERIMENT SETUP

Characterization of resistive and capacitive changes for humidity: Humidity-induced resistive and capacitive variations were studied for CPC sensors prepared at

various strain levels of 0.10, 0.12, 0.15, 0.18, and 0.24. The different specimens were placed at 35 %-RH for the first 20 seconds before supplying humid air for 50 seconds to achieve 100 %-RH. Note that a humidity chamber was not used to test a dramatic change of humidity. The outlet nozzle of humid air was located 10 mm above the top surface of specimen. Subsequently, humid air was removed to leave the sensor at RH 30% for 110 seconds. Therefore, the total time of experiment for each applied strain was 180 seconds. The resistance and capacitance values were measured by a Fluke meter and a capacitance meter (GLK 3000), respectively. The experiment was also repeated for resistive measurement (Fluke-287). Meanwhile, a commercial humidity sensor (DHT11-Temperature and Humidity Sensor) was located next to a CPC specimen for comparison.

Cyclic humidity test for a capacitive sensor: CPC specimen (5 mm width) with 0.24-strain were placed into a 3.8 L-chamber equipped with a humidifier and a vacuum pump. The humidity inside the chamber was monitored at a rate of 1 sample/s using a humidity sensor (DHT11). Cyclic experiments were conducted by varying the humidity within the RH ranging 37 ~ 100 % for 10 cycles. The evolution of the CPC capacitance values as a function of RH were recorded in real-time using a capacitance meter (GLK 3000).

To investigate the humidity sensing mechanism of a fractured CPC sensor, four different CPC sensors and one aluminum sensor were prepared (Table 3.1). Among the four different CPC sensors, a fractured CPC sensor was as prepared by 0.24-strain, a fractured sensor coated with polyacrylic acid (1 % - PAA), and a fractured CPC sensor laminated with a 20 μm-thick polyester film. The other was a CPC sensor trimmed with

scissors without fracture. An aluminum sensor was prepared by trimming a 100 μm-thick aluminum foil. All the surface area of one electrode was 5 x 5 mm2.

Table 3.1 Summary of the prepared humidity sensors

Sensor material	0.24-strain	Scissor trimming	Coating	Area (mm^2) / thickness (mm)
Fractured CPC	Yes	No	No	5 x 5 / 0.1
PAA-coated fractured CPC	Yes	No	1%-PAA	5 x 5 / 0.1
PET-laminated fractured CPC	Yes	No	PET film	5 x 5 / 0.1
Trimmed CPC	N/A	Yes	No	5 x 5 / 0.1
Trimmed Aluminum foil	N/A	Yes	No	5 x 5 / 0.1

The PAA-coated CPC was prepared to study if the swelling ability of cellulose fibers could enhance the capacitive sensitivity. 1% PAA-solution was deposited into a CPC sensor and cured for one hour on a hot plate. After curing, the sensor was fractured by introducing 0.24-strain. A fractured CPC sensor laminated with a polyester film was used to test sensitivity without direct contact to humidity. In comparison to a fractured CPC sensor without lamination, the response of a laminated sensor could give information about a sensing mechanism whether the sensitivity was resulted from the cantilever-shaped electrodes or the CNT surface change. A scissor-trimmed CPC sensor was used to study sensitivity without cantilever-shaped electrodes. Scissor-trimmed aluminum electrodes were fabricated in the same way as scissor-trimmed CPC electrodes. A scissor-trimmed

aluminum capacitance was prepared to study the CNT surface change in comparison to aluminum surface.

3.3 RESULT AND DISCUSSION

Characterization of resistive and capacitive changes for humidity: To investigate the resistive and capacitive changes to the humidity for various axial strains, the CPC samples with the applied strain of 0.1, 0.12. 0.15, 0.18, and 0.24 were exposed to RH 35 ~ 100 % (25℃). The 0.1-strain was an initial value because positive capacitance value was measured for a water-printed CPC specimen. Fig. 3.1 (b)-(f) show the resistive and capacitive changes for the humidity change. For the CPC with 0.10, 0.l2, and 0.15, the resistance gradually increased as the humid air was supplied and then reached to a plateau at 50 seconds. When the humid air was removed at 70s, the resistance increased again. As the applied strain was greater, the duration time of the increasing resistance value expanded. Under humid air, the resistance increase was originated from the swelling of fibers coated with MWCNTs due to water molecules. The hydroexpansion of cellulose fibers enlarged the distance between CNTs and break the percolation network which prevented electrical interactions among CNTs, therefore increased the composite resistance [73]. In our experiment, the resistance change was even greater because the auxeticity at fracture produced a greater water absorption through the larger surface area. Although humid air was removed at 70 s, the plenty amount of water molecules was absorbed and part of them left in the fibers. With the larger expansion, we observed a longer time of the second leap of the resistance increase.

The reason of the second leap was that, as the larger the axial strain was applied, the more surface area was generated because of the auxeticity. The longer time of resistance rise was achieved by swelling due to the extra amount of absorbed water molecules. It was interestingly found that the resistance values suddenly increased or decreased due to the fragile molecular junctions created by the broken fibers. The exposed fibers behaved as soft cantilevers, which were extremely sensitive to environmental intervention including humidity, pressure, and air flow. So, when high intensity humid air was supplied, the structure and shape of fiber network in the crack domain could be changed abruptly to change resistance for the samples with 0.12, 0.15 and 0.18 strain.

For the CPC with 0.24-strain, the specimen showed extreme binary characteristics between capacitance and resistance (Fig 3.1(f)). At this strain, the resistance was infinite but with the capacitance formation among very closely located fibers. For plotting purpose, the beginning point of resistance was set as 500MOhm, which was the maximum measurable resistance of the Fluke meter. Upon exposure to humidity, the resistance value decreased from infinity to a few MΩ because of water molecules trapping between fibers. Direct electric current flowed through water molecules upon humidity exposure. Without humid air, the junctions were not connected and behaved as a pure capacitor. According to the square input of RH-35~100 % humidity, the response time was 3s and the recovery time was 83s (Supplementary information, Fig. S4).

For the CPC samples at each strain, the capacitance showed relatively smooth transition. As soon as humid air was supplied, the capacitance increased. As soon as humid air was removed, the rising trend changed to a descending trend. Sometimes, a sudden drop of capacitance was shown due to temporary electrical connection with water vapor. Note

that the capacitance values for all the samples changed in the similar fashion but with different magnitude. The magnitude of the capacitance change due to the humidity was descending with the larger axial strain. The peak values of capacitance were 2.98, 3.94, 2.22, 0.88, and 0.45 pF for the CPC specimen with 0.1, 0.12, 0.15, 0.18, and 0.24-strains, respectively. The highest capacitive sensitivity of CPC sensor was at 0.12-strain, which was right after fracture.

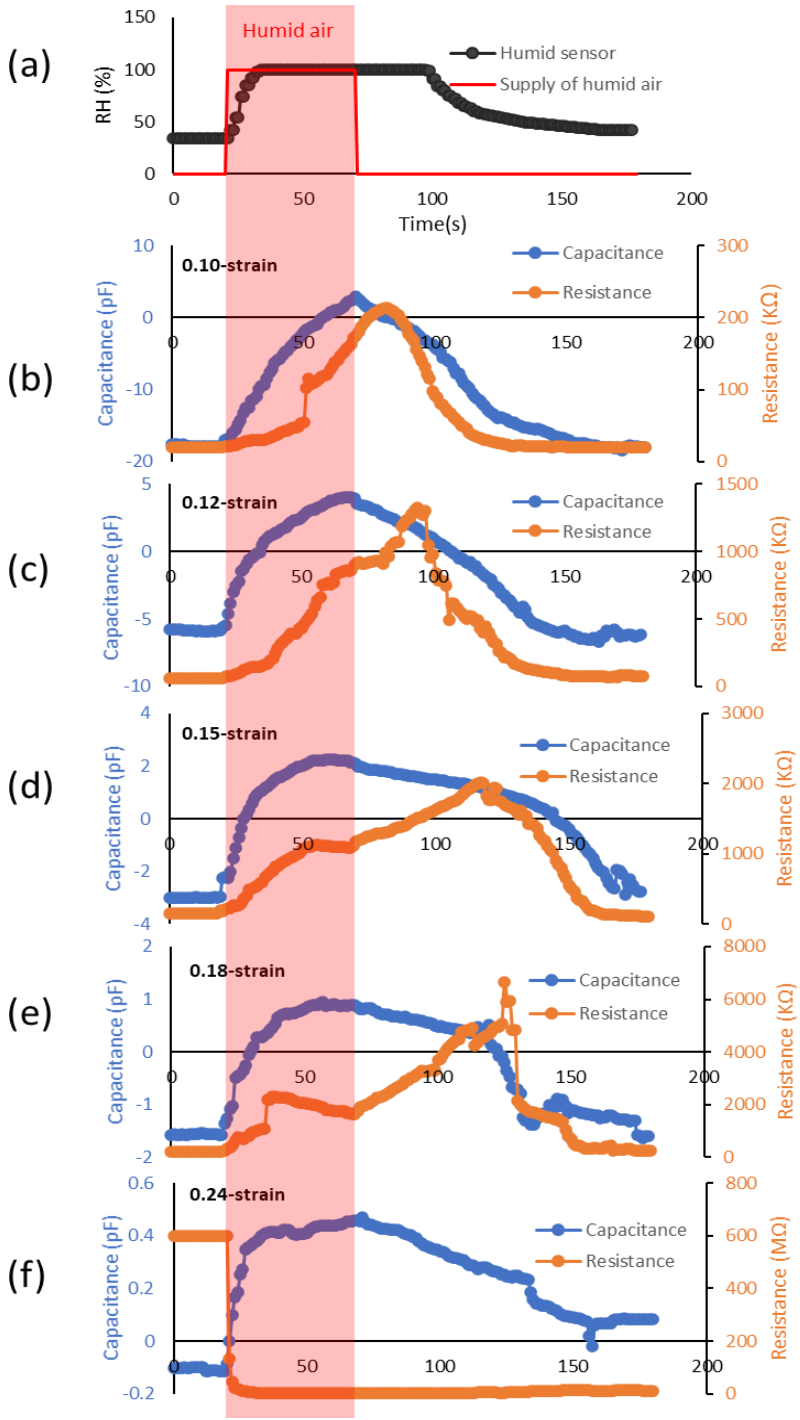

Figure 3.1 (a) Programmed humid air and detected humidity change (b) ~ (f) Capacitive and resistive characteristics for CPC specimens with 0.1, 0.12. 0.15, 0.18, and 0.24-strains.

Cyclic humidity test for a capacitive sensor

Fig. 3.2a shows the capacitance change for a CPC humidity sensor for the first four cycles of RH 40~90 %. Except for the first cycle, the measured capacitance values were stable and reproducible. The normalized capacitance change ($\Delta C/C_0$) at the tested RH was 0.47±0.03 pF. During the humidity test, the temperature change was less than 1 °C. The capacitive change due to the temperature change could be neglected.

Fig. 3.2b shows the normalized capacitance change ($\Delta C/C_0$) for the cyclic test of RH 40~90 % (N=6). Based on the graph, the empirical equation (r^2 = 0.93) between the normalized capacitance value and the relative humidity was:

$$RH = 106.6x^{0.1778} - 6x \quad (3)$$

where x is the normalized capacitance value ($\Delta C/C_0$).

When a staircase input of humidity was given, the response was similar to that of a commercial sensor (DHT11) (Fig. 3.2c). The CPC sensor gave a more rapid response to the humidity change at the beginning and followed the similar trend to a commercial sensor. In comparison to other capacitive humidity sensors, the normalized capacitance changes $\Delta C/C_0$ in the RH range of 40%-80% as well as the materials of the capacitive humidity sensors were summarized in Table 3.2. Since the conventional capacitive humidity sensors were fabricated in the form of a dielectric layer between two electrodes. Some researchers put their efforts in modifying the dielectric layer to be more water sensitive, while others worked on the electrodes through coating or changed the capacitance type from metal-insulator-metal to interdigitated electrodes (IDE). For the modification on the dielectric media in between of the two metal plates [74-77],the sensitivity was relatively linear and

the normalized change of capacitance $\Delta C/C_0$ is small. However, the thin film coating [78] on the electrodes will drastically increase the change of capacitance when RH level was elevated because of the capability of water sorption and the interaction of water molecules. If the electrode type switched from metal plate to IDE, with additional coating material [79-81], the sensitivity was increased drastically and nonlinearly. Gsaper and Olkkonen used the inkjet-printed on a paper substrate as the humidity sensor in their study. The $\Delta C/C_0$ of their sensor was good and linear with respect to the RH change, however, the response time humidity step from 40 to 100 RH% was 250s while our CPC sensor was 3s. Another type of capacitive humidity sensor was cylindrical parallel plate with a modified hydrophobic material in between [82, 83], but the capacitance change of this type of sensor was even smaller.

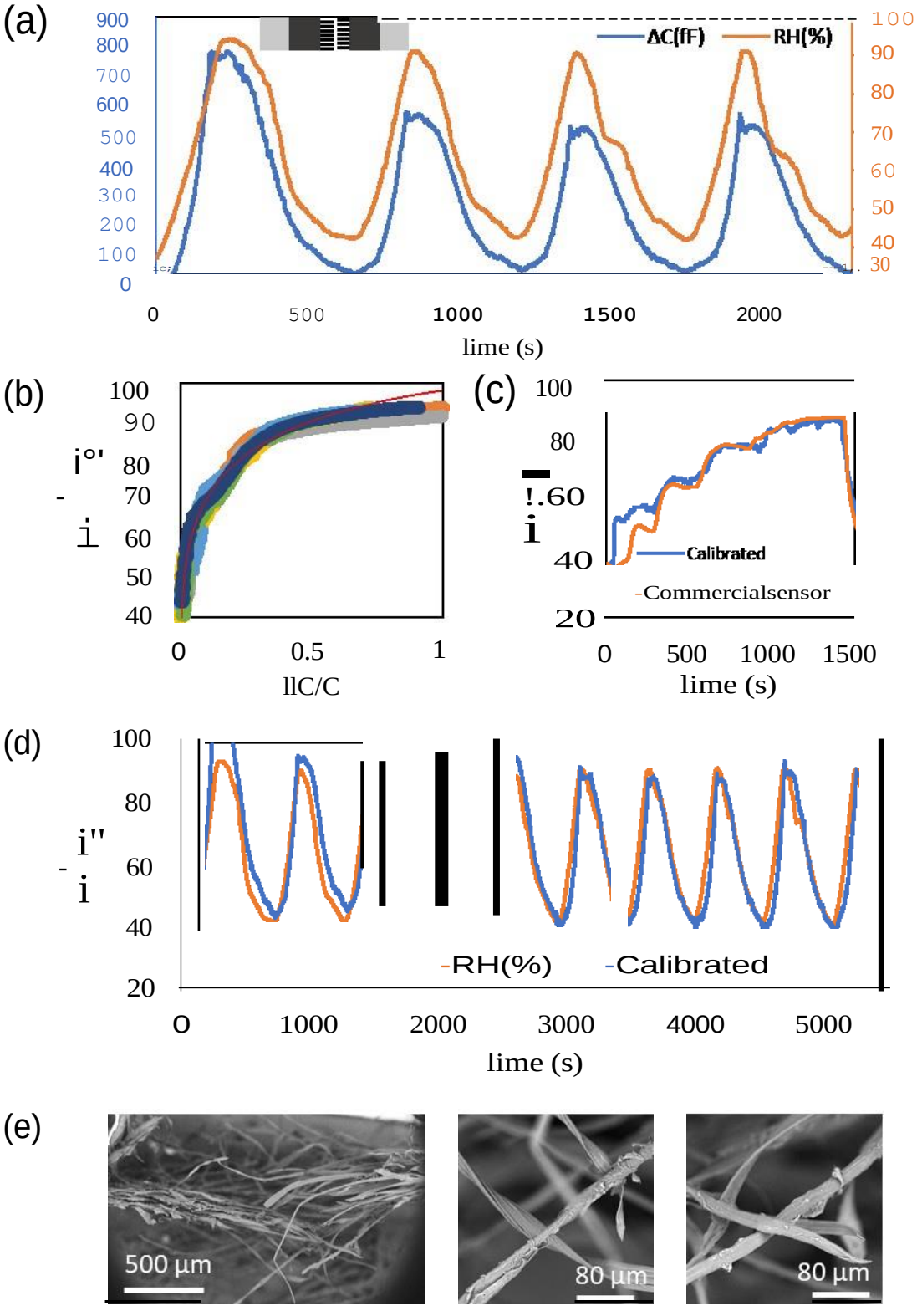
(a)
900
800
700
600
500
400
300
200
100
0
100
90
80
70
60
50
40
30
ΔC(fF)
RH(%)
0
500
1000
1500
2000
lime (s)
(b)
100
90
80
70
60
50
40
0
0.5
1
llC/C
(c)
100
80
60
40
20
Calibrated
-Commercialsensor
0
500
1000
1500
lime (s)
(d)
100
80
60
40
20
-RH(%)
-Calibrated
0
1000
2000
3000
4000
5000
lime (s)
(e)
500 µm
80 µm
80 µm

Figure 3.2 (a) Capacitance change of a fractured CPC sensor according to cyclic humidity change. The 5mm-wide CPC sensor is made of 0.24-strain. (b) The relationship between RH and $\Delta C/C_0$ (N=6). The red line shows the empirical equation. (c) Comparison of a CPC sensor response to a commercial sensor response for the staircase input of humidity. (d) Comparison of calibrated fractured CPC-humidity response to a commercial sensor for 10 cycles. (e) SEM images for a CPC sensor fractured with 0.24 strain. Molecular crossing junctions to detect humidity.

In general, our CPC sensor showed a relative great sensitivity in terms of the normalized capacitance $\Delta C/C_0$ without a medium between CPC electrodes. Meanwhile, the structure and the process of fabricating our CPC sensor was less complicated than the sensors showed in the references.

Fig 3.2d shows the comparison between the calibrated RH data of a CPC sensor using equation (3) and the RH data measured by the reference humidity sensor, which showed a good agreement. Also, six additional sensors were tested for four humidity cycles in order to evaluate the reproducibility (Supplementary Information, Fig. S6). For the measurement obtained after the initial cycle, the sensor response became repeatable and stable.

The high capacitive sensitivity of the fractured CPC composite to the humidity resulted from the molecular junctions made by the large auxetic behavior. The major contribution of auxetic behavior was to form crossing molecular junctions among radial crossing structures (Fig 3.2e), which produced an extreme capacitive sensitivity to humidity. The molecular junctions were newly generated capacitance from the randomly oriented fiber network through water printing and wetting. When the junctions were exposed to water vapor, the water molecules adsorbed at the junctions worked as the media

with high permittivity. At higher strain values, the gap between fibers increased, hence reducing the sensitivity. For example, when the molecular junctions were eliminated with a 1 mm distance between the electrodes, the high sensitivity to humidity disappeared.

Table 3.2 Comparison of capacitive humidity sensors

	$\Delta C/ C_0$ (RH 40~80%)	Electrodes and dielectric medium
CPC	0.225	Electrode: fractured CPC (0.24 strain) medium: none
Ref. [74]	0.15	Electrode: metal medium: bis(benzo cyclobutene)
Ref. [75]	0.10	Electrode: Au film medium: carbon black polyimide
Ref. [76]	0.09	Electrode: Aluminum medium: polyimide
Ref. [77]	0.05	Electrode: Au layer medium: polyimide
Ref. [81]	0.015	Electrode: Interdigitated textile electrode coating: Metal-Organic Framework layer
Ref. [79]	0.25 40-65% 75 65-85%	Electrode: Interdigitated textile electrode coating: crystalline trianglamine hydrochloride

Ref. [80]	350	Electrode: coplanar interdigitated electrodes coating: nanostructured TiO_2 thin films
Ref. [78]	0.5	Electrode: Aluminum layer medium: $Cu_3(BTC)_2$ film
Ref. [84]	0.08	Electrode: PET substrate coating: Ag electroplating with Ni or Parylene-C
Ref. [85]	1.8	Electrode: Paper substrate coating: Printed silver interdigitated
Ref. [82]	0.04	Electrode: Copper coating: Graphene oxide coated silk fiber
Ref. [83]	0.016	Electrode: Copper coating: graphene (G) in polyvinylidene fluoride

To elucidate the capacitive sensing mechanism of humidity, three more CPC sensors were prepared as shown in Table 3.1; CPC sensors coated with PAA, a polyester film, and trimmed with a scissor. A metallic capacitive sensor was also prepared by trimming a 100 μm-thick aluminum foil with the same dimensions. Fig 3.3a shows the capacitance change of a fractured CPC coated with PAA. The PAA-coated CPC sensor showed the multistage swelling effect. When contacting water vapor, both PAA and fibers could swell with hydroexpansion, which showed the phase shift. The magnitude of capacitance change was ~ 100fF, which was much smaller than the CPC sensors without

PAA coating. The hysteresis potentially caused by the swelling effect became greater to reduce the capacitive change for repeated cycles. Therefore, the capacitive response of fractured CPC was not originated from the swelling effect but could be resulted from the capacitive change on the MWCNT surface of the fractured fibers.

A scissor-trimmed CPC sensor without fracture (Fig 3.3b) showed ~ 10fF in the given humidity range. The fractured CPC coated with a PET film showed the change of 20fF because the adsorption of water molecules was blocked by a plastic film (Fig 3.3c). The sensitivity was higher than those of a trimmed CPC sensor due to the higher electric field strength and the larger surface area generated by the high aspect ratio CNT coated fibers. The metallic capacitive sensor showed a 10fF change similar to the trimmed CPC sensor (Fig 3.3d).

The high capacitive sensitivity of the fractured CPC composite to the humidity was resulted the molecular junctions made by the large auxetic behavior. The major contribution of auxetic behavior was to form crossing molecular junctions among radial crossing structures, which produced an extreme capacitive sensitivity to humidity. The molecular junctions were completely newly generated capacitance from the randomly oriented fiber network through water printing and wetting. When the junctions were exposed to water vapor, the water molecules adsorbed at the junction worked as the media with high permittivity. At higher strain values, the gap between fibers increased, hence reducing the sensitivity. For example, when the molecular junctions were eliminated with 1 mm distance between electrodes, the high sensitivity to humidity disappeared.

For humidity sensing, resistive and capacitive sensors are commercially available. Between two electrodes, a humidity absorption pad is applied to change resistance or

permittivity to capacitance. Using CNTs, a humidity sensor was investigated for a resistive sensor due to the changes in sorption of water molecules [86]. The resistance change of CPC coated with PAA was also sensitive to humidity due to a swelling effect [87, 88]. The fractured CPC capacitive sensor was novel in that the capacitive change to humidity was significant without a dielectric medium. A capacitive sensor using air as a medium did not function due to negligible permittivity change of air in humidity. The high electric field and the large surface area contributed to the sensitive measurement to humidity. When the fractured fibers coated with CNTs were blocked with a polyester film, the humidity change was still detectable but a reduced sensitivity. The experimental results showed that the major capacitive response was resulted from the change of CNT surface on cellulose fibers. The molecular junctions of a fractured CPC sensor created a significant capacitance change without a dielectric medium, which facilitated a highly sensitive capacitive sensor as shown in Table 3.2.

The capacitive sensing mechanism of fractured CPC composite was investigated and tested for humidity. The auxetic behavior created the crossing junctions of the high aspect ratio-cellulose fibers to enhance the electric field and surface area around the crack domain. Water molecules introduced on the surface of the crossing radial structure enlarged the capacitance change among the high aspect ratio electrodes, resulting in the extreme change of capacitance. The large capacitance change was resulted from the auxetic behavior caused by the buckling of a specimen. The sensitivity of the sensor due to RH cycles was observed in the controlled humidity chamber and calibrated with a reference humidity sensor. According to the test results, a capacitance reached a maximum value where the fracture of the CPC composite was just occurred. The magnitude of Poisson's

ratio was also the maximum at the point. An empirical equation for the capacitance value and RH curve was obtained by calibration with a reference humidity sensor. The calibrated fracture CPC humid sensor could also be used for sweating measurement in our hand. Hence, the fractured CPC capacitive sensor is capable of sensing humidity without absorption medium because the auxetically-produced cantilever shaped electrodes form very sensitive capacitive junctions. The capacitive sensing platform will facilitate a wearable sensor detecting humidity and moisture change.

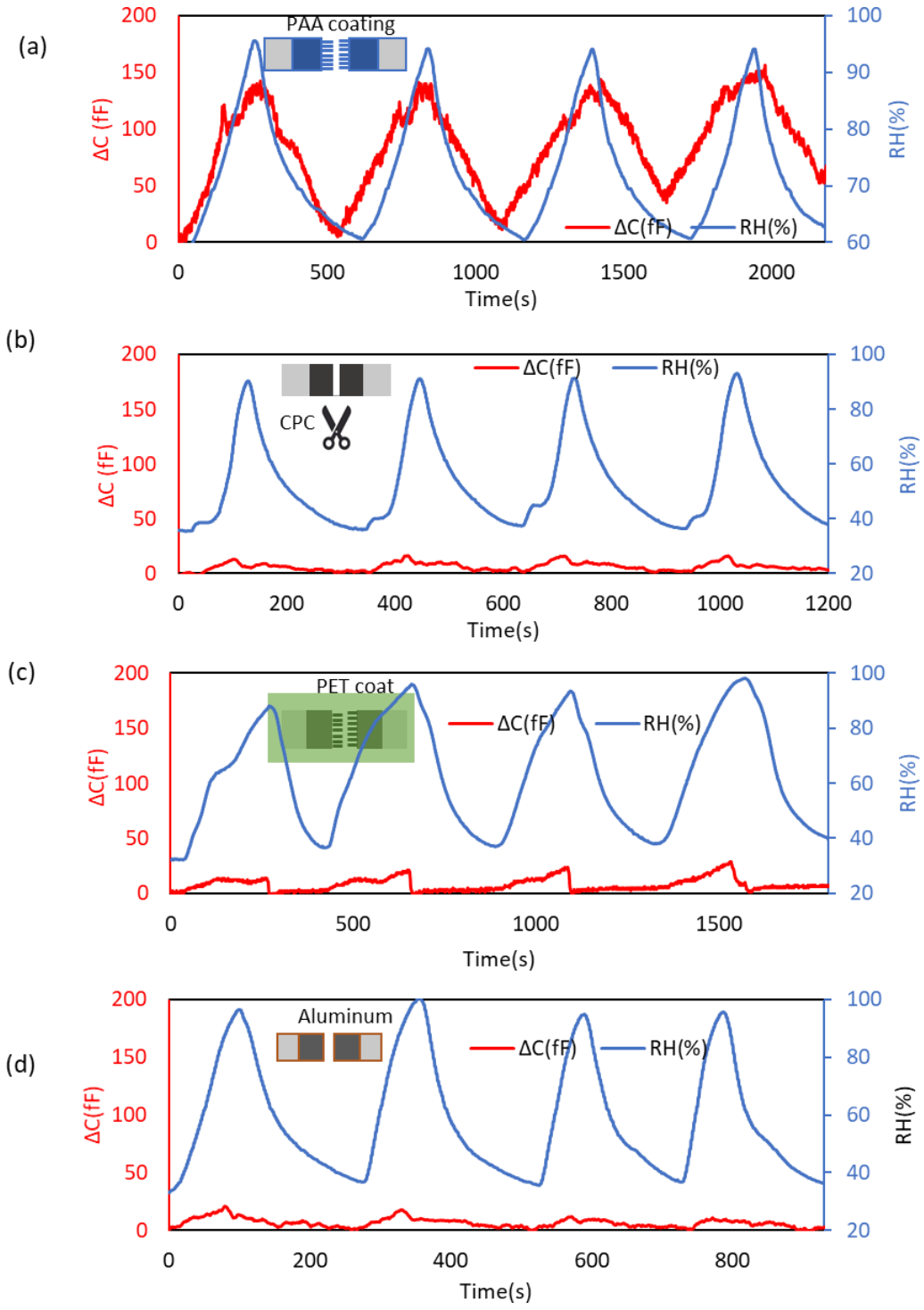

Figure 3.3 Capacitive changes of (a) PAA-coated fractured CPC, (b) trimmed-CPC, (c) PET film-coated fractured CPC, and (d) trimmed aluminum sensors for cyclic humidity change.

3.4 APPLICATION OF CPC HUMID SENSOR

A fractured CPC sensor with 0.24-strain could be used to evaluate the sweat evaporation of a human's skin. To test a CPC sensor, a small chamber with an evaporation hole to contain a commercial humidity sensor and a CPC sensor was constructed (Fig 3.4a).

When a CPC sensor was placed in the center of the palm, sweat evaporation was detected from a human hand. The data obtained from a CPC sensor were measured using a capacitance-to-digital chip (FDC1004) that was controlled by a microprocessor (Atmega 328). The RH reached 85 % when the chamber was placed on the palm, which decreased to a room RH-55% when the sensor was removed from the palm. The calibrated humidity data for CPC were compared to those of a commercial sensor (Fig 3.4b). The calibrated data showed good agreement with the reference commercial sensor. In the experiment, the sensor chamber was grounded with an aluminum foil to avoid the interference from the human body and other environmental noises. Using the electrically isolated chamber, the selectivity to humidity could be obtained.

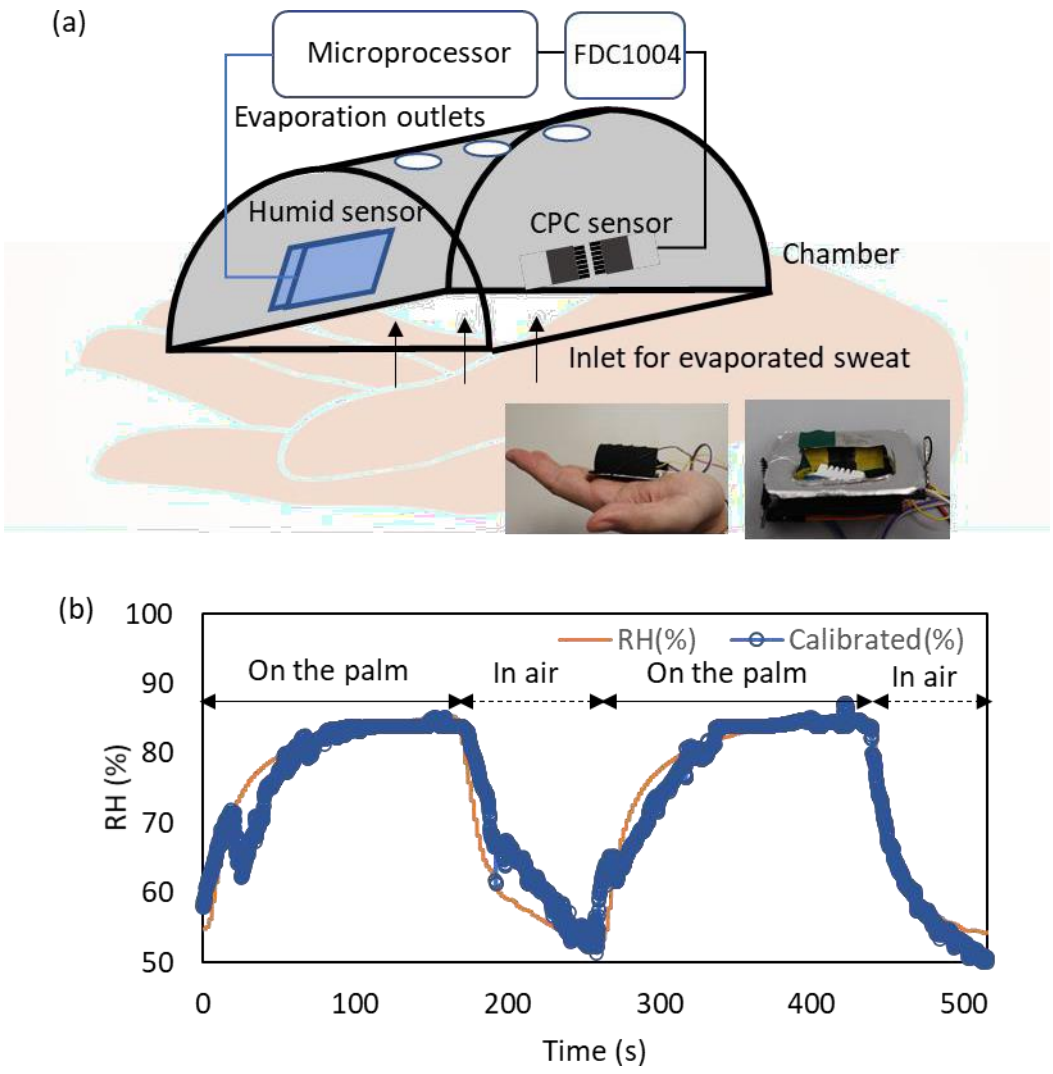

Figure 3.4 (a) Chamber to measure humidity change on a hand. A commercial humidity sensor is integrated with a fractured CPC sensor. To eliminate the parasitic capacitance from a human hand, the chamber is covered with an electrically grounded aluminium foil. The test has been conducted multiple times only for one subject. (b) Capacitance change is measured on the palm and in the air. The humidity change of a capacitive CPC sensor shows a good agreement with that of a resistive commercial sensor. The study related to sweat monitoring was approved by the institutional review board (IRB) at the University of Washington (IRB ID: STUDY00010741). The sensor characterization was conducted according to the approved procedure under the consent of the study participants.

3.5 CONCLUSIONS

The capacitive sensing mechanism of an auxetic CPC composite was investigated under varying humidity conditions. When a water-printed CPC composite was stretched, the auxetic behavior produced the radial structures of cellulose fibers embedded with MWCNTs. The high aspect ratio fibers of fractured CPC generated crossing junctions at the crack of the water-printed region. Water molecules introduced on the surface of the crossing radial structure enlarged the capacitance change among the high aspect ratio electrodes, resulting in the extreme change of capacitance. The normalized capacitance change ($\Delta C/C$) for a CPC humid sensor was 0.225 in the relative humidity ranging 40~80 %. Since the auxetic behavior was enlarged with the buckling on the out-of-plane direction of a CPC composite, the larger width generated a 40 times capacitance in comparison to the capacitance of the planar metal electrodes of the same dimensions. According to our further analysis, the capacitive sensitivity to humidity was originated from the crossing molecular junctions of conductive fibers that trapped water molecules. Due to the molecular junctions, a large change of capacitance could be obtained without a humidity absorption pad. An empirical equation between capacitance and RH was obtained by calibration with a reference humidity sensor. The CPC-capacitive sensor could be used for sweating measurements on the hand. The auxetically produced capacitive sensing platform can facilitate a wearable sensor measuring humidity and sweat.

Chapter 4. LIQUID DETECTION USING CAPACITIVE SENSOR

4.1 INTRODUCTION

Liquid detection involving the measurement of liquid dielectric properties, level, and flow rate has been important for various daily, environmental, and industrial applications. As the need of real-time and simple liquid detection grows, a low-cost and user-friendly sensor has been demanded for liquid profiling in a container or pipe. Waveguide systems [89] and resonance sensors [90] have been frequently used in the detection of the liquid dielectric properties. However, the methodological constraints including sample placement [91] hinder the applications. Liquid level can be measured by pressure [92], optical [93], ultrasonic [94], or electrical sensors [95, 96]. A hydrostatic pressure sensor is an inexpensive option [92]. Since the sensor requires contact to liquid, which can increase flow resistance, liquid contamination, and inconvenience in installation. Optical and ultrasonic sensors have been featured as noncontact sensors without the risk of contamination [93, 94]. Despite the benefits, these methods are expensive and error-prone due to by external noise [97]. The electrical sensors such as resistive and capacitive sensors can be a cost-effective option [95, 96]. However, the resistive sensors are only applicable to conductive liquid while requiring relatively high power [95]. Capacitive sensors have been regarded as a promising instrument to detect the level of both conductive and insulating liquid with high sensitivity and low power requirement. The detection capability of dielectric constants could be an additional benefit [96].

To date, capacitive liquid detection has been studied for detecting liquid level, dielectric constants, and flow rate [98, 99]. The capacitive sensors are sensitive to the dielectric property and level of liquid [100]. The interdigitated electrodes (IDE) could be used to sensitively detect the degree of oil deterioration due to the varying dielectric constants [101, 102]. The sensitivity of 24 pF per unit dielectric constant could be achieved. However, the sensor was required to be immersed in oil, which hampered the non-contact applications. IDE was also utilized to detect the water content in the soil with the accuracy of 5% of water content [103]. A capacitive probe was developed to detect the different dielectric constants of liquid [104]. However, the dynamic range was narrow, resulting in the signal saturation over 32 of a dielectric constant. Nevertheless, the aforementioned sensors could only detect the properties of the liquid near the sensor's surface. For liquid level detection, multiple sensors were required, which was cumbersome for actual use.

Coplanar electrodes were used for capacitive sensors, where fringing field generated higher capacitance signal [105]. Capacitive electrodes were attached to the bottom or the side of liquid container for level measurement. For the lateral sensor placement, the electrodes were attached outside the wall of the container, where the capacitance increased as the liquid covered larger area of the sensor [106-108]. The resolution of 0.1 mm could be achieved [106]. However, larger electrodes were required to cover the whole lateral wall. For the bottom placement, the electrodes were placed outside and under the container to measure the liquid level and dielectric properties [109-112]. IDE were developed and placed under a microfluidic device to measure the liquid level [109]. Using the micro-gap between electrodes, three different dielectric liquids including distilled water, glycerol, and tetraethylene glycol could be differentiated. The

dynamic range of 0~200 μm (liquid level) and the resolution of 10 μm could be achieved. According to previous results, there was a trade between dynamic range and resolution, which was correlated to the electrode gap size. For example, the improved dynamic range of 0~1.5 mm made the resolution 0.1 mm [112]. Due to the fringing effect [105], a smaller electrode gap showed a higher sensitivity but a reduced dynamic range. A larger electrode gap had wider dynamic range but lower sensitivity [109, 111-113]. Assuming only one electrode sensor having an infinite gap size, the dynamic range may be much larger due to the diverging electrical field [114].

The non-contact capacitive sensors were also studied to measure a flow rate in a tube [115-119]. According to the numerical simulation, laminar flow could shape a dynamic electrical double layer (EDL) due to a parabolic velocity profile [115], causing capacitance change. Orifice capacitive sensors were developed to measure flow rate [116, 117]. Various flow velocity profiles could generate different turbulent regions after passing the orifice. Since the dielectric constant in the turbulent region was smaller in comparison to the central region, the difference could be detected. However, the method was only applicable to high flow rate (~10 L/min). Also, monitoring two-phase flow (gas-liquid or solid-liquid) was intensively studied [118, 119]. Since the dielectric properties of the liquid and gas were significantly different, the sensors could measure the velocity of air bubbles to estimate liquid flow rate.

In this chapter, a liquid sensor made of carbon nanotubes-paper composite (CPC) is studied to measure the liquid level. Our study focuses on a single electrode sensor to investigate the capacitive interaction between liquid level and environment. The differential measurement of liquid is studied to enhance sensitivity and stability. This

capacitive sensor could rapidly and constantly detect the liquid level with high sensitivity in a non-contact manner. Moreover, this sensor could be applied on various kinds of containers including glass and metal. The dynamic range and liquid level detection accuracy will be evaluated in the contexts of femtofarad level-accuracy of capacitance. The single electrode configuration incorporating the simple form factor will facilitate various applications, such as vending machine, water leak detector, rain detector, food processor and industry automation.

4.2 THEORY AND SIMULATION

The capacitive sensor configuration for liquid level sensing was either parallel or co-planar. In the parallel setup (Fig 4.1a), the electrode dimension was the same as the container dimension to cover the full range of the liquid level. Although only one pair of electrodes could cover the level, the resolution was compromised. As for co-planar placement (Fig 4.1b), two electrodes were placed in a very small gap where the high electric field was generated due to the fringe effect. In this configuration, the penetration depth (T) of a co-planar capacitor was calculated in equation (4.1). Within the range of T, the liquid level was able to be detected accurately. However, the depth depending on the small gap size could limit the sensing range to the vicinity of the sensors.

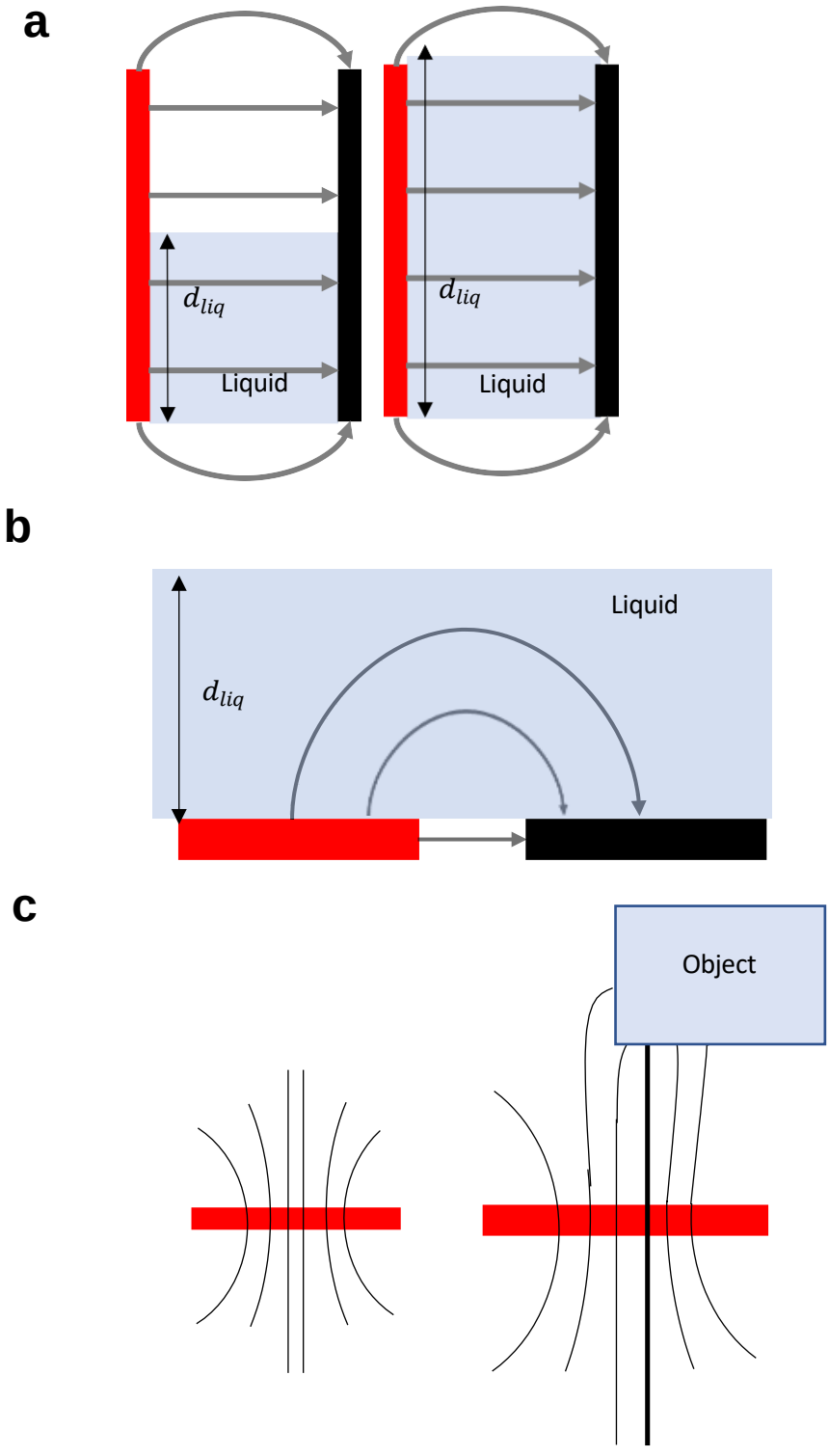

Figure 4.1 (a) Parallel capacitor for liquid level detection. (b) Co-planar capacitor and the dynamic range. (c) Self-capacitance measurement

$$T = asinh\,[cosh^{-1}\,(1 + \frac{w}{a})] = a\sqrt{(1 + \frac{w}{a})^2 - 1} \quad (4.1)$$

According to the equation (1), as the gap size increased, the penetration depth increased with reduction of the accuracy. Without losing accuracy, the dynamic range of water level could be improved by employing an array of electrodes or interdigitated electrodes. However, such measurement configuration was not suitable for industrial and commercial applications. To address this challenge, we proposed to use a single electrode that was made of carbon nanotube paper composite (CPC). The single electrode was used in a self-capacitive system that measured the capacitance change with respect to the earth ground (Fig 4.1c). Considering the conventional capacitor composed of excitation- and grounded electrodes, the second electrode in self-capacitance was regarded as ground or an object. If an object approached the electrode, the capacitance would increase. When a single electrode was employed, the theoretical penetration depth became infinite, which could be calculated in equation (1) by assigning the gap size an infinity. The CPC electrodes were fabricated from tensional fracture [120]. The fractured electrodes created an array of cantilever-shaped electrodes mimicking interdigitated electrodes (IDE). The high aspect ratio structure created large surface area to enhance the fringing electric field and thus the capacitive sensitivity.

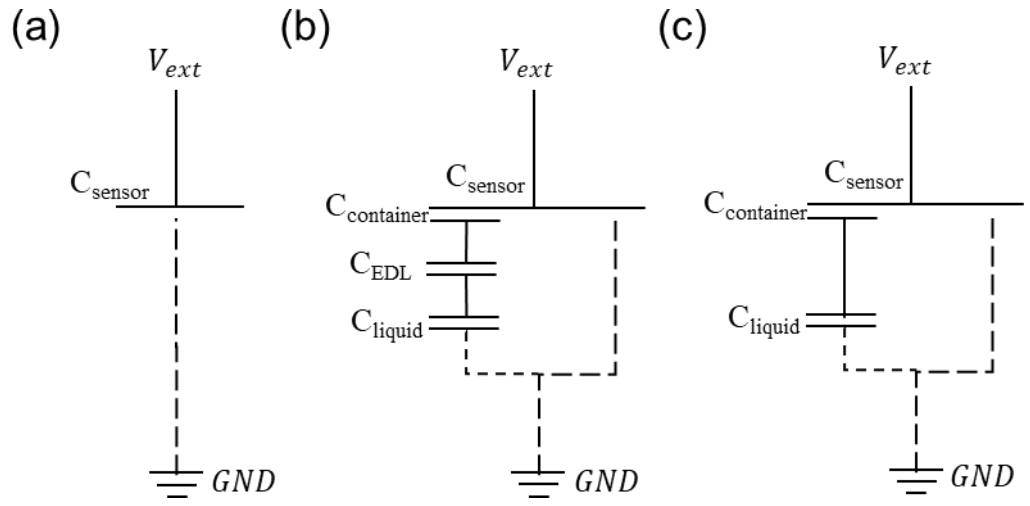

Figure 4.2 Mathematical model for the single electrode capacitive sensor system of (a) A single electrode capacitance sensor without an object. (b) A sensor with a container and liquid. (b) Simplified sensing model of liquid in a container

For liquid level detection, the single electrode self-capacitance measurement was modeled in Fig 4.2. The sensor is powered by the excitation voltage and the initial capacitance is determined with surrounding ground that is expressed with the dotted line (Fig 4.2a). Liquid introduction in the container increased the initial interaction between the sensor and surrounding ground by adding a series of capacitors into the system (Fig 4.2b). The mathematical model is given as:

$$C == C_{self} + \frac{1}{\frac{1}{C_{container}} + \frac{1}{C_{EDL}} + \frac{1}{C_{liquid}}} \tag{4.2}$$

where Cw, CEDL, and Cself are the capacitances of liquid, electrical double layer, and self-capacitance. The self-capacitance forms between the excitation electrode and the environmental ground. Considering the thickness of the electrical double layer 1~100nm, the large capacitance of C_{EDL} could be eliminated in the serial capacitances. The simplified capacitance configuration is given by Fig 4.2c.

For a single electrode capacitor, electric field distribution through liquid was studied by numerical analysis. The capacitance change, $\Delta C = (C_1 - C_0)$ was used as a parameter, where C_1 and C_0 were the capacitance values with and without liquid, respectively. Both containers made of non-conductive glass- and conductive stainless steel were modeled to study the electric field and the resulting capacitance change. The sensor was modeled as a rectangular shape metal plate whose dimension was 5x5x1 mm^3. The gap size between the sensor and the container was 1 mm (Fig 4.3). Two numerical models were constructed to investigate the sensing mechanism of liquid in the conductive and non-conductive containers respectively.

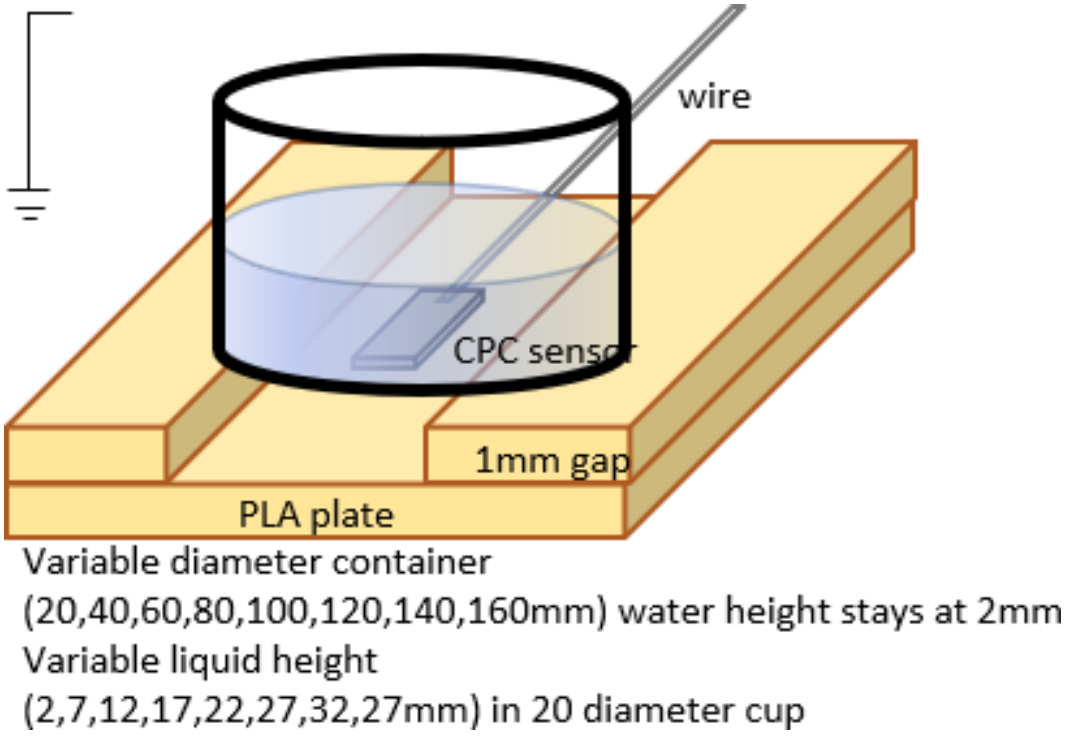

Figure 4.3 Schematic diagram for the setup of the simulation and experiment validation of single electrode capacitive sensing for liquid detection

4.2.1 *Numerical results for a non-conductive liquid container*

One test was to investigate how the diameter of the container would contribute to ΔC. The liquid level in this study was 2mm, and the container diameter varied from 20mm to 160mm with the step of 20mm. The relative permittivity of the liquid was 80. A 5V AC potential at 10 kHz frequency was applied on the electrode. The sensor and container were all encapsulated in a grounded cube with the 100mm length. The entire system can be modeled as shown in Fig 4.4.

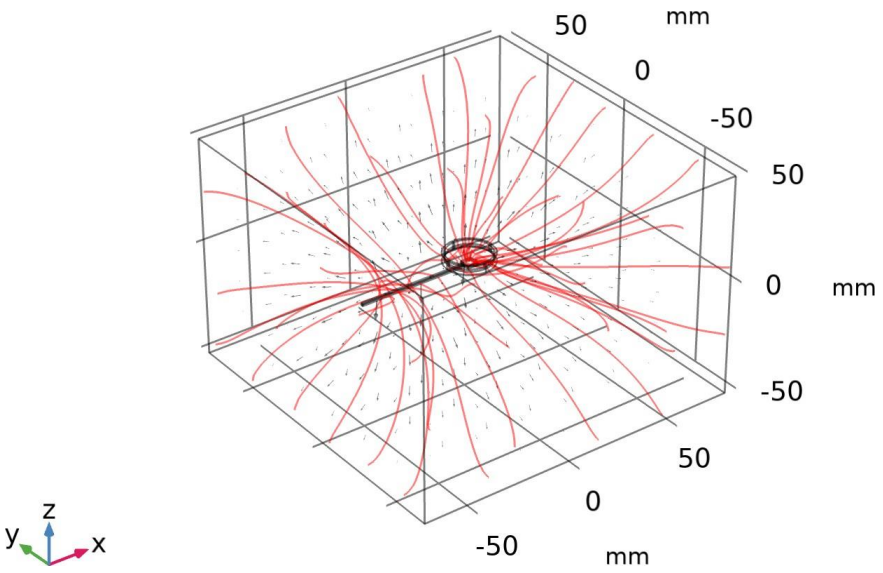

Figure 4.4 Sensor and cup were encapsuled in the grounded box

The electric field and the capacitance were computed for each diameter. Another test was focused on the liquid level when the container diameter was 20mm. The water level ranged between 1 and 13mm with a 1mm step.

The electric field fringed from the sensor as well as the wire to the grounded box. The electric field was distributed from the sensor to the ground without liquid. When liquid was introduced, the electric field distribution was changed to increase ΔC. Fig. 4.5 showed the electric field in terms of both streamlines and gradient ramp. From the gradient format, it was found that the electric field strength between water and sensor was higher and decayed toward the whole rectangular cage. The introduced liquid formed a capacitance with the single electrode. The electric field distributed between the side area of the liquid in the glass container and the grounded box. For an empty cup, the single electrode formed the capacitance with the grounded box regardless of the container size. When liquid was introduced, the capacitive system became a bit more complicated. Each surface of the liquid in the container formed a capacitor together with either the sensor or the surrounding grounded walls.

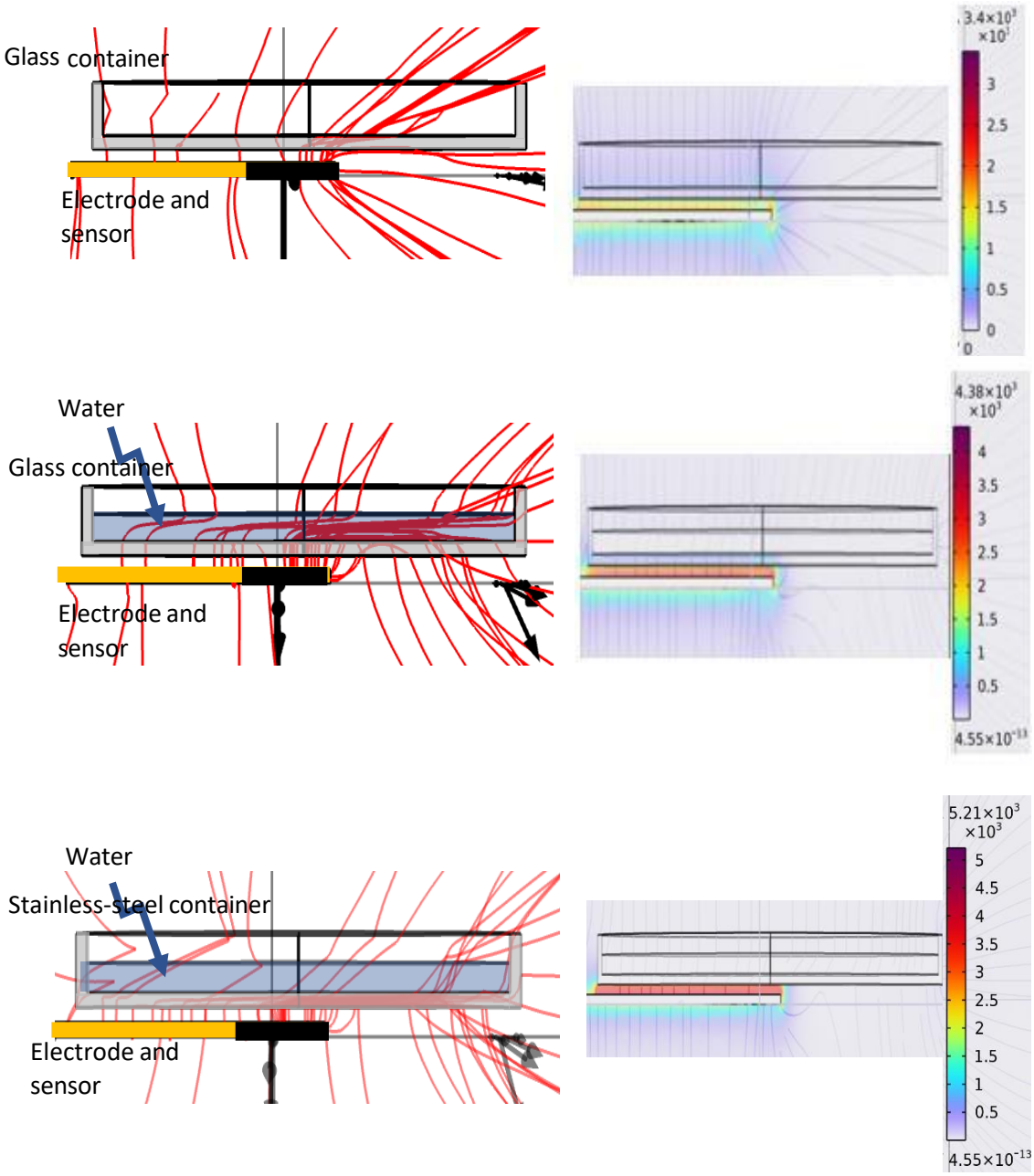

Figure 4.5 Electrical streamlines (left) and gradient (right) results for empty glass cup, filled glass cup and filled stainless-steel cup in simulation

4.2.2 *Numerical results for a conductive liquid container*

The simulation for conductive container liquid test was focused on the liquid level with the container having 40 mm-diameter. To estimate ΔC, the C_0 of empty stainless-steel cup was located on the single electrode. The numerical study was conducted for the different liquid levels in the cup. ΔC was computed based on C_0.

According to the electric field distribution (Fig 4.5), capacitance formed between the metal cup and the electrode. As shown in the figure of simulation, the additional liquid could not change the electrical distribution in the container because the charges from the sensor would be transferred to the conductive cup and then distributed to the grounded box. Therefore, ΔC was negligible due to liquid level increase.

4.3 MATERIALS AND EXPERIMENTAL METHODS

4.3.1 *Fabrication of the single-ended sensor*

In this paper, the single-ended capacitive sensor was made of carbon nanotube paper composites (CPC) reported in the previous research [120]. The sensor was fabricated by trimming the CPC material to 10x5 mm^2 square shape. Through the wet-stretching method, 5x5 mm^2 fibrous pieces of CPC were fabricated.

4.3.2 *Measurement setup and capacitance measurement circuit*

The setup was plotted in Fig 4.6. Since our capacitive sensor worked with a single electrode, the excitation voltage was applied to the fibrous CPC electrode that was located at the bottom of the 3D-printed U shape stage. The ground electrode was present only on a capacitance chip. The distance of the excitation electrode and the container bottom was 0.5mm in order to avoid the pressure effect. Since the fibrous electrodes had conductivity of 1 S/m, the resistance decreased upon pressure, which in turn increase the capacitance value. To study the charging effect, the pressure effect was negated by applying an air gap between the excitation electrode and the container bottom.

The measurement circuit consisted of a capacitance to digital converter (CDC). A CDC chip (Analog Device, AD7747) generated the excitation frequency of 16kHz to measure the capacitance. The chip offered a high resolution of 0.1 fF. Also, the capacitive chip allowed the measurement of self-capacitance using a single electrode. Using two channels, differential measurement could be conducted to measure the capacitance of a sensing electrode in comparison to a reference electrode. For the initial test, single-ended

configuration was used to test the capacitance change in comparison to the numerical study. Differential measurement was employed to obtain a high accurate capacitive measurement by canceling the environmental noise. The sampling rate of the AD7747 converter was 45Hz, which allowed us to obtain reliable averaged data.

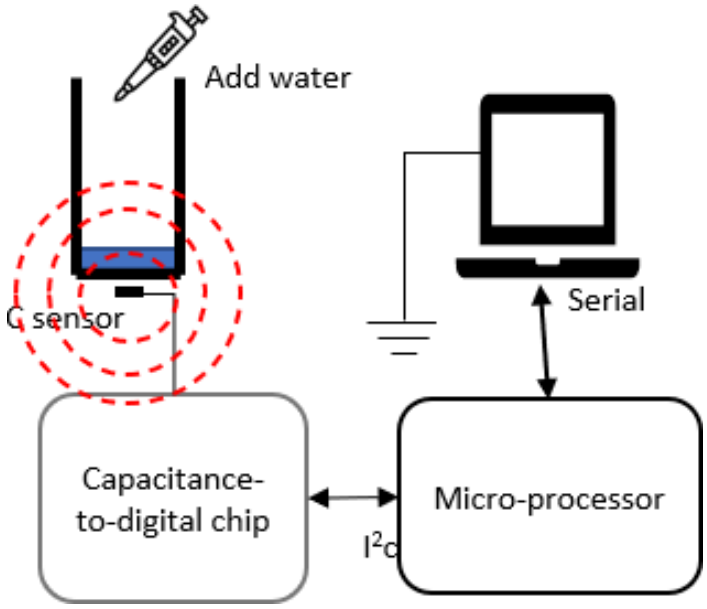

Figure 4.6 Schematic diagram of the measurement system

4.3.3 *Capacitive characterization for various container dimensions*

To validate our numerical study results, the experimental setup was constructed to resemble the numerical model. Using a 3D printer, the various diameters of containers with the same height were printed to measure ΔC depending on the bottom liquid area. In the tests, a single-ended configuration was used. The capacitance of each printed cup was measured under two conditions, without water and with a certain volume of water which filled the cup to the level of 2mm. The values of these two conditions were recorded as C_0

and C_1. Then the capacitance change ΔC of the experiment was obtained from ($C_1 - C_0$) and compared with the ΔC of simulation.

A 30mm inner diameter glass beaker was employed to compare the result of simulation for liquid level detection. In this test, two kinds of electrode were considered, one was the fibrous CPC sensor, the other was a copper plate which was in the same size of 5x5 mm^2 to check if the normal metal electrode had the approximate performance as CPC. ΔC was measured for each electrode for the same beaker and water volume.

A set of small radius cups (3, 4, 5, 6, 7, and 8 mm) were fabricated to measure ΔC by filling with the small volume of water. 100μL was added to the cups by each step until the total volume became 1mL. The liquid tests of a large volume were conducted using large volume glass beakers. Four diameter glass beakers (25, 47, 72, and 102mm) were used for large volume measurement.

4.3.4 *Capacitive characterization for water volume and area*

The same volume of water was dropped on a glass plate and a Teflon plate to observe ΔC. Teflon was chosen because a water drop was pinned without spreading. Water drop spread on hydrophilic glass surface. Since both Teflon and glass were nonconductive, ΔC could be induced by the water area facing to the sensor. Before experiment, the base capacitance value of each plate was measured as C_0. Water was dispensed in four steps. The capacitance of each step was measured and subtracted by C_0 to obtain the ΔC. First, a 100 μL of water was dropped on each plate. Three more 10 μL of water was sequentially added to the original drop. The results of the two plates were compared.

4.3.5 *Characterization of conductive container and dielectric constants using differential measurement*

ΔC values of different liquid or solutions were compared to test the sensitivity to dielectric constants. Since the dimension and the volume of the liquid caused ΔC, the differential configuration using two capacitive sensors was employed. Two fibrous CPC sensors were placed with 30mm-distance to alleviate the electric field interference. The whole measurement setup was enclosed in a grounded box in order to reduce the external noise. (Fig 4.7.a, b) In the configuration, a control sensor was covered by the reference cup while the liquid volume on a sensing electrode was replaced.

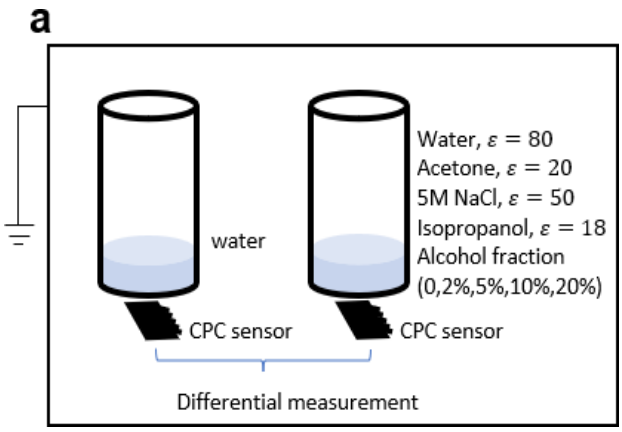

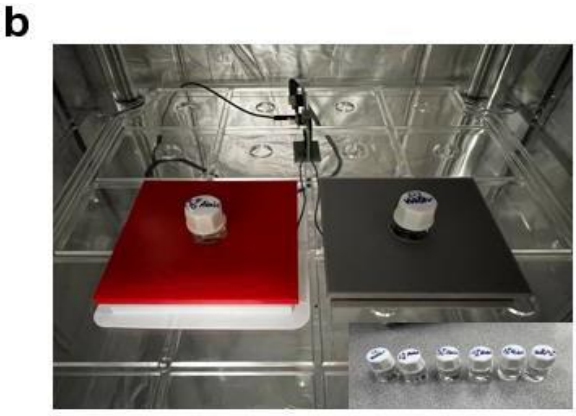

Figure 4.7 (a) Sketch of experimental setup of differential measurement for conductive container and dielectric property tests. (b) Pictures of differential measurements for two solution comparison.

To proceed with the differential measurement, the first critical issue was whether the reference container should be filled with liquid or not. Two sets of tests using non-conductive cups were conducted, one was using an empty cup as reference and the other used the filled cup. The sensing cup for the two sets started with empty and followed by adding 5 steps of same volume water. Standard deviation of each step was calculated and compared.

The 1mL cylindrical glass vials were used for testing liquids. Since the capacitance was sensitive to geometry and location, two same holders of the vials were fabricated and attached to the stage, which was in the middle of the electrically grounded box. Initially, water was compared to water in order to test the error of ΔC. Theoretically, ΔC between two water bottles should be 0fF. Subsequently, the bottle on a sensing electrode was replaced with the same volume of 5M NaCl solution, acetone, and isopropanol.

Furthermore, the volume fraction of alcohol in water was changed to measure ΔC to test the sensitivity. A series of alcohol fraction solutions between 0 and 15% were tested in comparison to water.

4.4 RESULTS

4.4.1 *Capacitive response to non-conductive container*

Both bottom and side areas of the container increased ΔC when water was introduced. The bottom area dominated ΔC, meaning that the initial introduction of water increased ΔC significantly due to the charge transfer to the initial water volume. Fig 4.8.a compares the ΔC of different diameter cups with the same liquid level of 2mm. Every point was calculated by subtracting the capacitance value in the water-supplied cup by the capacitance value of an empty cup. The experimental results agreed well with the simulation results. Based on the figure, ΔC was proportional to the cup diameter at a fixed small height. The liquid level was maintained at 2 mm in order to study how the bottom area changed the capacitance signal. The water level of 2mm was the minimum height to overcome the surface tension and make the entire bottom surface of the PLA container wet. If the liquid volume did not completely cover the entire bottom surface, ΔC was impacted by the drop shape. In the experiment, ΔC was dominated by the bottom area.

Fig 4.8b displayed the relationship between ΔC and the liquid level with a 30mm diameter- bottom surface. In this test, as more liquid was supplied into the container, the slopes of ΔC increased for both simulation and experiment were almost the same. Through the simulation, the ΔC for each step of level increment became smaller as the absolute liquid level became higher.

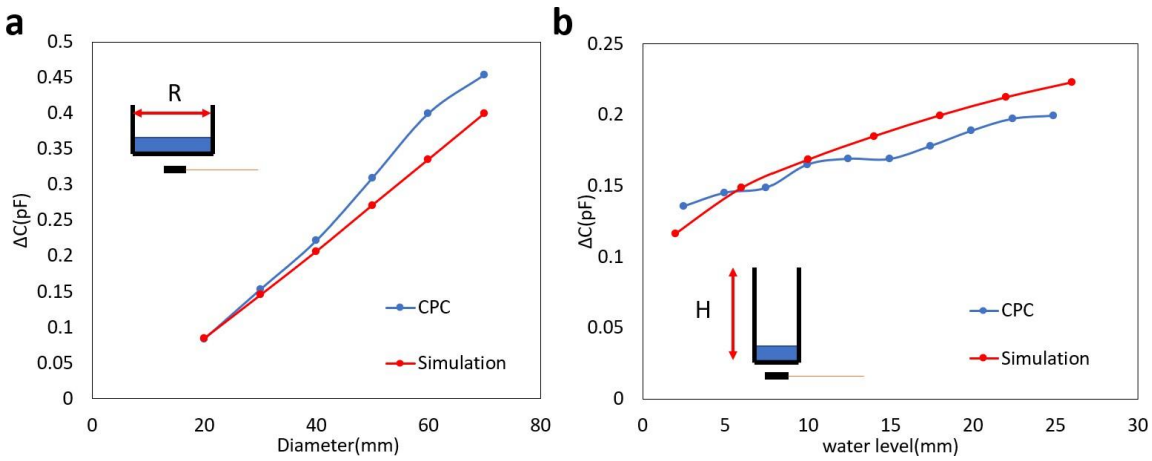

Figure 4.8 (a) Simulation and experiment results for variable diameter non-conductive containers. (b) Comparison of results of simulation and metal, CPC electrode in liquid level measurements.

4.4.2 *Capacitive response to conductive container*

For the conductive container, we chose to use stainless-steel cups. Since the ΔC with and without water was only a few femtofarad. To improve the signal to noise ratio, the differential measurement setup in Fig 4.9a was employed, which could confine the peak to peak noise capacitance below 0.2fF.

Compared to the non-conductive container, we noticed that C_0 value for a stainless-steel cup was much higher than that of the PLA cup. The ΔC of adding the same level of liquid in metal cup was much smaller. In simulation, we obtained the results showing that the ΔC for the water level below than 20mm was fluctuating in Fig 4.9b. showing the numerical errors. In experiments, the differential configuration was able to measure the ΔC at real time by placing the other stainless-steel cup on the reference sensor. The capacitance was measured for both cups simultaneously to cancel the environmental disturbance. The

result of experiment showed a quadratic increase of ΔC which was only a few femtofarad. The numerical and experimental results agreed that ΔC became larger when liquid level was close to fill the entire bottle. Recall the result of the liquid level for the non-conductive container, the trend of the curve of ΔC with respect to liquid level was opposite to the trend of stainless-steel cup. For non-conductive cup, the empty container did not change the electrical paths. Once the container started to be filled, it began to behave as the second electrode and interact with the sensor and the ground.

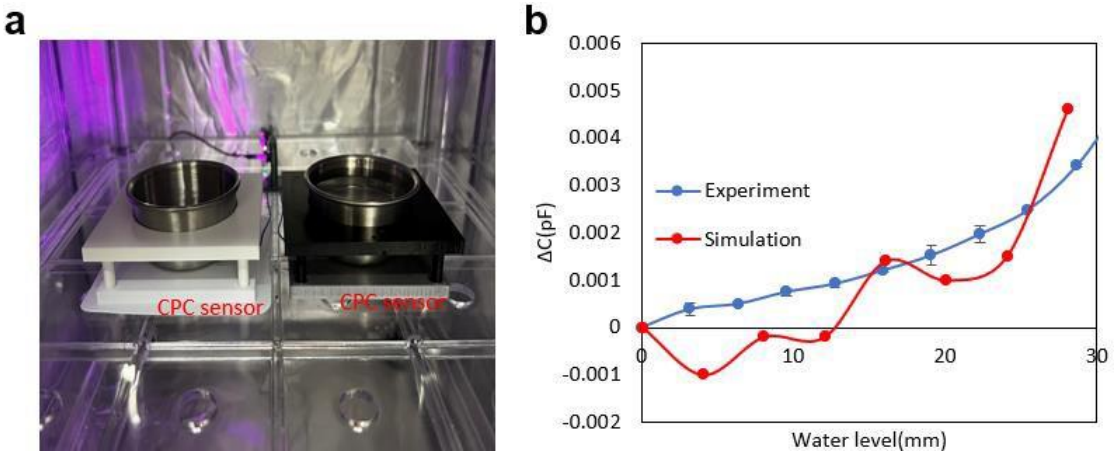

Figure 4.9 (a) Experimental setup of differential measurement for liquid level detection of conductive containers. (b) Comparison of simulation and experiment results.

4.4.3 *Model for ΔC and dimension*

Various radius cups (3, 4, 5, 6, 7, and 8mm) were examined to determine the general model for the relationship between the ΔC and liquid levels in the single electrode sensing system. Single-ended configuration was chosen to measure the capacitance values.

Fig 4.10a displayed the result of ΔC for different diameter containers with respect to filling the same amount of liquid each step. All cups generated corresponding curves that distinguished from each other, which were reflected by the slope. The ΔC for the first dropping water varied slightly for each cup since 100μL of water was not enough to cover the entire bottom surface of the cup. The spreading area for each droplet was not able to cover the identical area. It was obvious that each curve had two slopes and a turnover point, indicating that the bottom area was filled. After this turnover, the ΔC was linearly increased at each step.

Fig 4.10b was the truncated figure of Fig 4.10a after the turnover point according to the liquid volume, which depicted the ΔC from the side area increment. Due to the various diameters of cups, the slope of ΔC with respect to volume was different. The ΔC of a 3mm diameter cup was the largest among all the testing cups since the area increment was the largest for a 3mm-cup when same volume of water was added. Based on the results, the sensitivity of each dimension of the cup could be calculated. The sensitivity with respect to the liquid volume as well as the sensitivity with respect to liquid level were all obtained and shown in Fig 4.10c and d which indicated the potential design method of the container for various purposes. If the liquid volume was the requirement, then the high aspect ratio cup was the option which gave us the sensitivity of 1.36fF/μL. A large diameter

container was more appropriate for measuring the liquid level. In our test, the sensitivity of 8mm cup could reach to 6.5fF/mm.

Besides the small diameter and volume containers, large glass beakers were tested with our single fibrous CPC sensor as well. Fig 4.10e and f displayed the ΔC with respect to liquid level and the added water volume. Unlike what we observed from the small cups, the relationship was no longer linear when the liquid exceeded 100mm. With the increase of the water level, the ΔC continuously increased but the increment could be less than the previous increment as we expected from the simulation. This ΔC decay was more obvious when the liquid level passed 100mm. When the level was beyond 400mm. the ΔC increase was almost negligible which gave us the approximate dynamic range. Similar to the small diameter cups, the large beaker also exhibited that when high sensitivity of liquid level was required, larger diameter was preferred. A smaller diameter container achieved higher resolution in terms of the volume measurement.

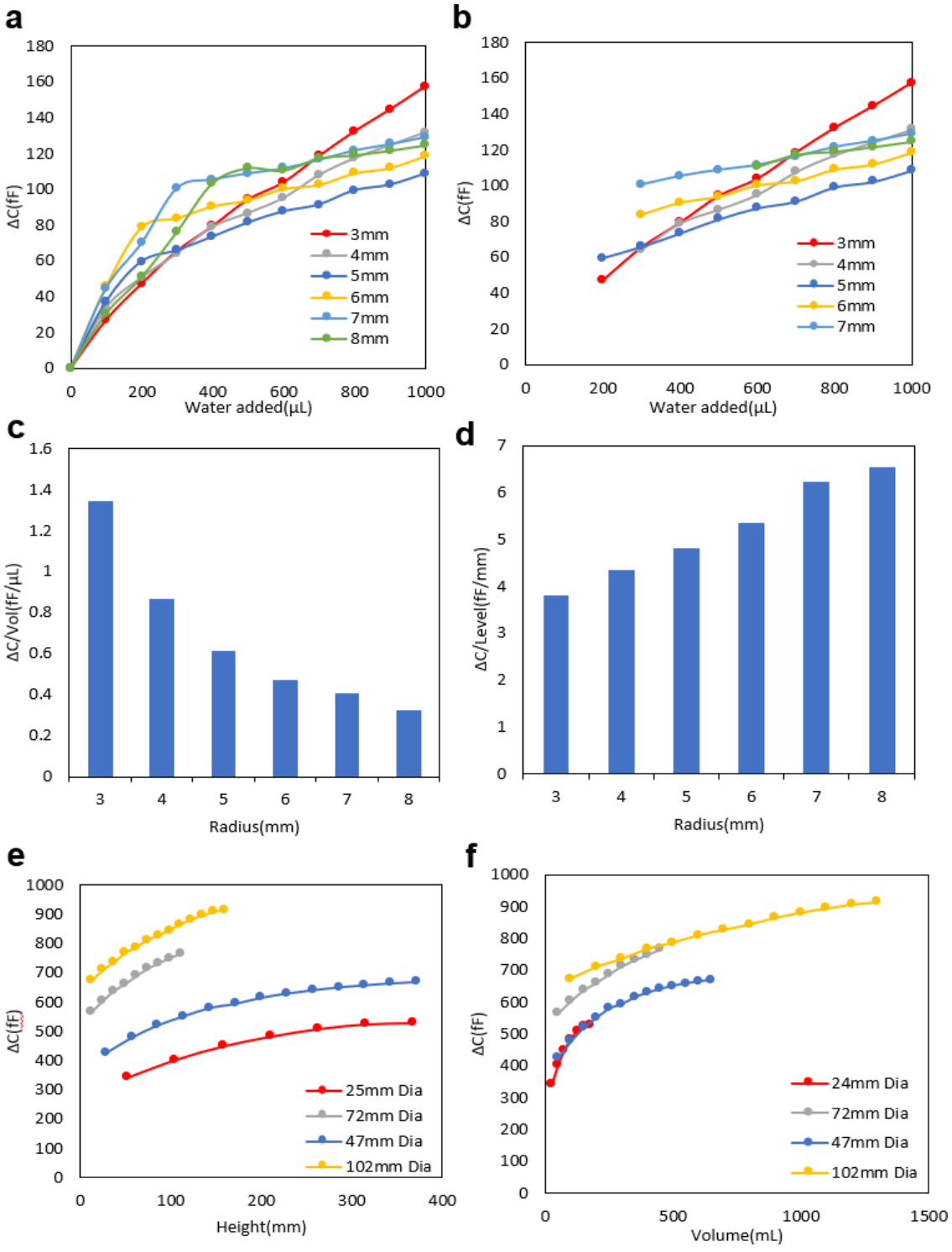

Figure 4.10 (a) Capacitance change of variable PLA cups with respect to the volume change. (b) Capacitance change for volume change after filling the bottom area. (c) Sensitivity of single electrode CPC sensor in terms of liquid volume for various radius

non-conductive containers. (d) Sensitivity of single electrode CPC sensor in terms of liquid level for various radius non-conductive containers. (e) Capacitance change with respect to liquid level for large diameter beakers. (f) Capacitance change with respect to liquid volume for large diameter beakers.

4.4.4 *Engineering model for the non-conductive container*

The model based on the 1mm wall thickness small diameter non-conductive container was calculated to predict the liquid level through the known dimension of the cup and the corresponding ΔC in Equation 4.3.

$$Water\ level = \frac{\Delta C}{(5.663 * R + 2.06)} \tag{4.3}$$

The results of the prediction based on the model and experiments were calculated and compared for the radius of 3,5 and 7mm width containers in Fig 4.11. From the comparison, the model exhibited a good performance in terms of liquid level prediction. However, the model could only be applied to this series of containers. If the material, wall thickness and the test setup were changed, further characterization and calibration were necessary to obtain the specialized model parameters.

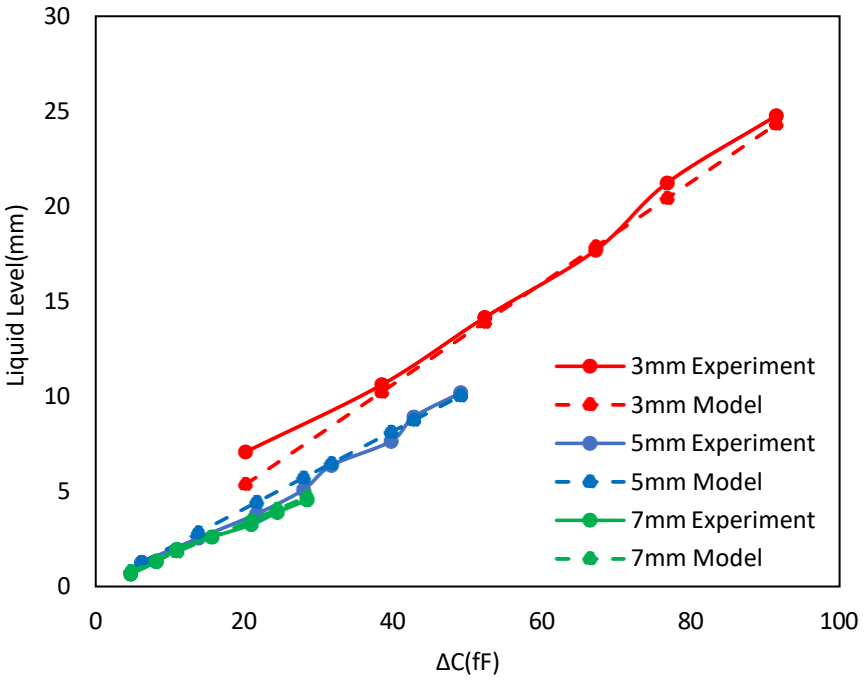

Figure 4.11 Comparison of the results of prediction model and experiments.

4.4.5 *Characterization of volume and area*

The capacitive response signals of the same volume of water drop on glass plate and Teflon plate were compared. Because of the hydrophobic property of Teflon, the drop was hinged to limit the horizontal area. However, the water on the hydrophilic glass plate could expand randomly, which enlarged the facing area to the sensor. Based on the result in Fig 4.12, the ΔC for the same volume of water on glass plate was greater than that on Teflon plate. Additionally, after the first drop, 3 more 10 μL of water was added in sequence. The ΔC of glass plate kept increasing but the ΔC was not significant on Teflon plate. From this test, it was concluded that the majority of the ΔC was contributed by the surface area of the liquid. And when the liquid object was closer to the sensor, the higher sensitivity could be achieved.

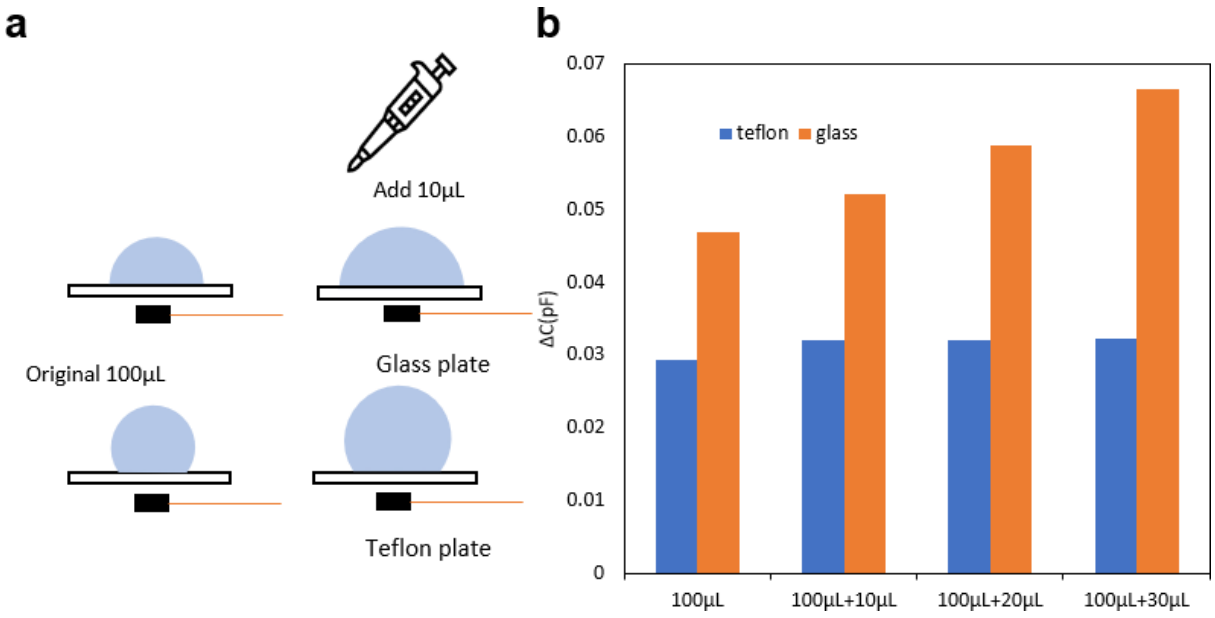

Figure 4.12 (a) Procedures of the test of adding water droplets on the glass and Teflon plates. (b) Comparison between capacitance change of glass and Teflon test.

4.4.6 *Differential measurements for dielectric constant*

Since the single electrode in the self-capacitive sensing system is fringing to the all surrounding ground, it is easily affected by environmental interferences. The noise level of the single-ended configuration was expected to lower the accuracy and resolution. In order to overcome the disturbance, the differential measurement configuration was employed. Fig 4.13a showed the sketch of the differential setup in which two identical sensors as well as the containers were used as two pairs. One sensor and container were regarded as the reference which was set at the beginning of the test while the other pair worked as the sensing group in which the variable liquid level was added. The measurement result was the difference of the capacitance change between the two sensors.

Because these two sensors measured at the same time and test environment, the ambient disturbance was compensated by the difference calculation.

The material in the reference container was calculated and discussed in Fig 4.13. For the empty bottle as reference, the noise level was almost higher than 0.2fF. When using filled container as reference, the noise level could maintain at the range around 0.1fF unless the sensing side was empty since the filled water worked as the second electrode which created strong and stable fringing field between the sensor and the container.

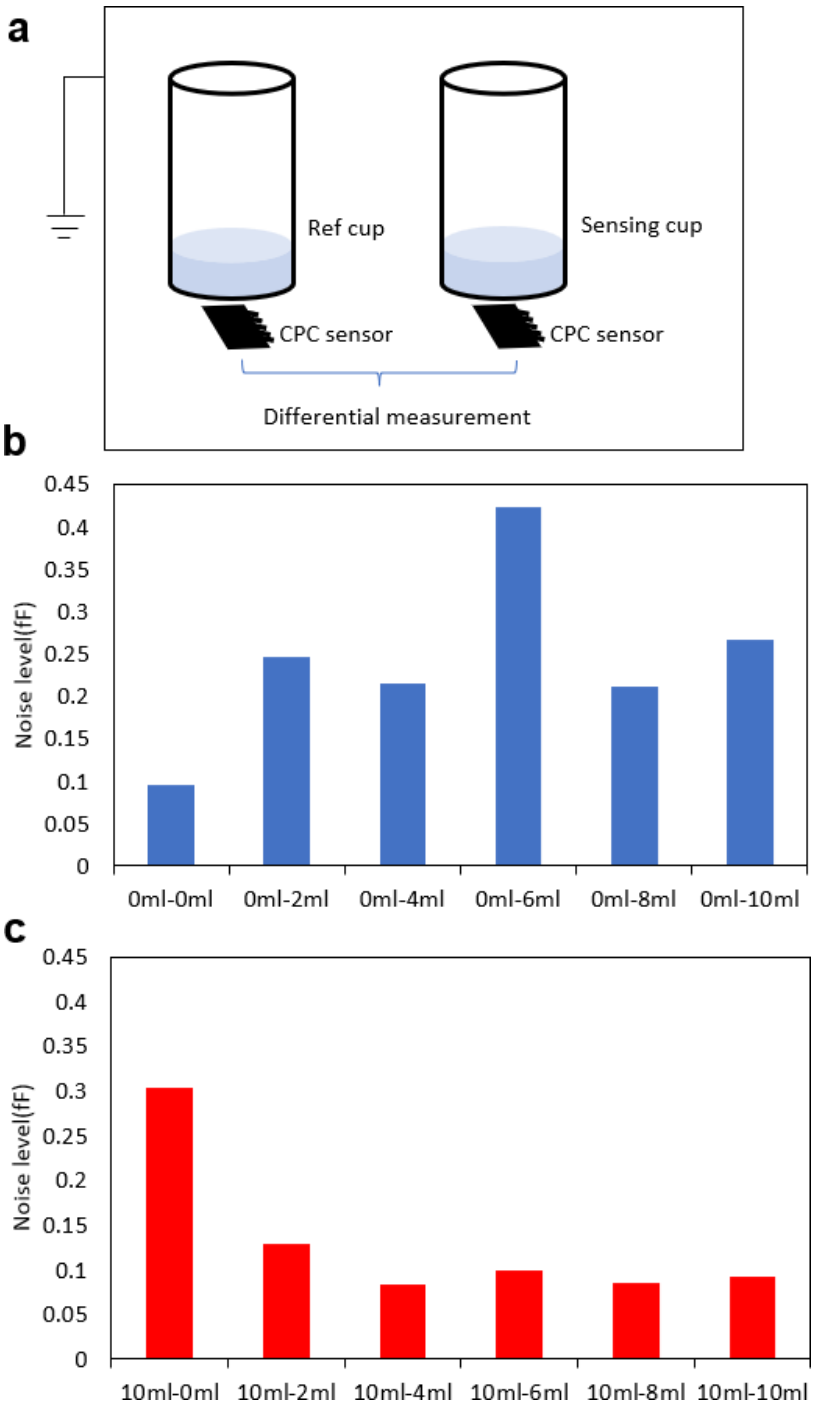

Figure 4.13 (a) Schematic diagram for differential measurement configuration (b) Noise level test result for empty cup as reference. (c) Noise level test result for Liquid-filled cup as reference.

Fig 4.14 described the difference of the capacitance value with respect to the dielectric constant of the specific liquid. All the liquids were filled into the identical containers with the volume of 1mL. The water-to-water comparison was first tested to understand the noise level. From the result, the ΔC was larger as the dielectric constant discrepancy between two liquids diverged. Meanwhile, the result also indicated that the ΔC was proportional to the dielectric constant of the liquid if the dimension of the two comparing objects was the same.

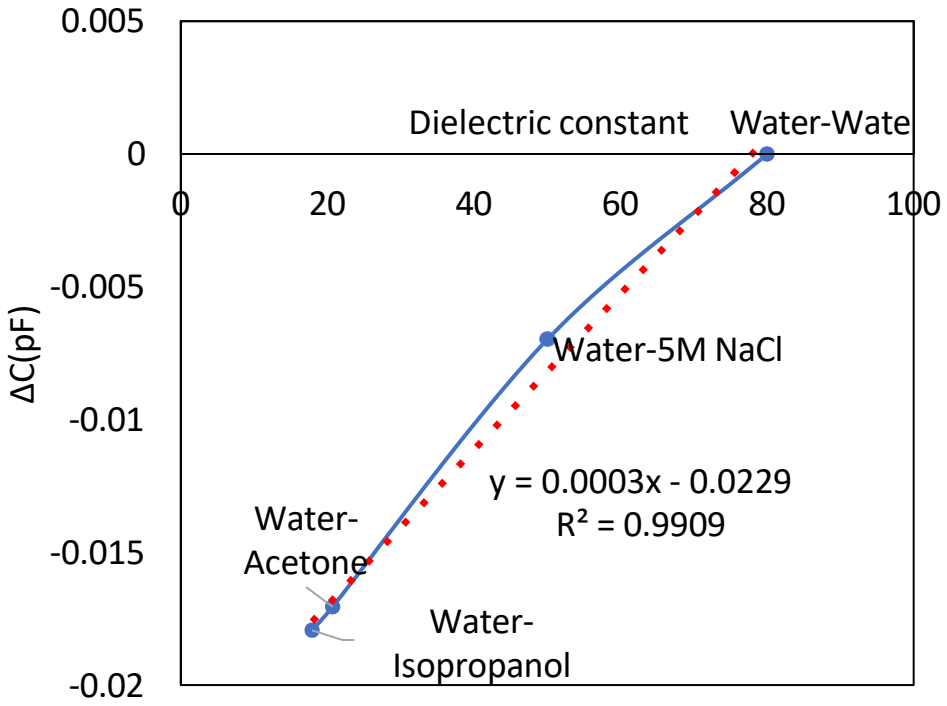

Figure 4.14 Capacitance difference between solutions with different dielectric properties and water

Fig 4.15 depicted the change of ΔC and the volume fraction of alcohol. Similar to the previous test, the 0% alcohol solution was compared first to calibrate the measurement. As more alcohol added to the solution, the ΔC increased accordingly and linearly. Since

the dielectric constant was reduced by the alcohol, the relationship could be modeled to calculate the volume fraction of the alcoholic solution. In comparison to the noise level, the resolution was 1%-alcohol.

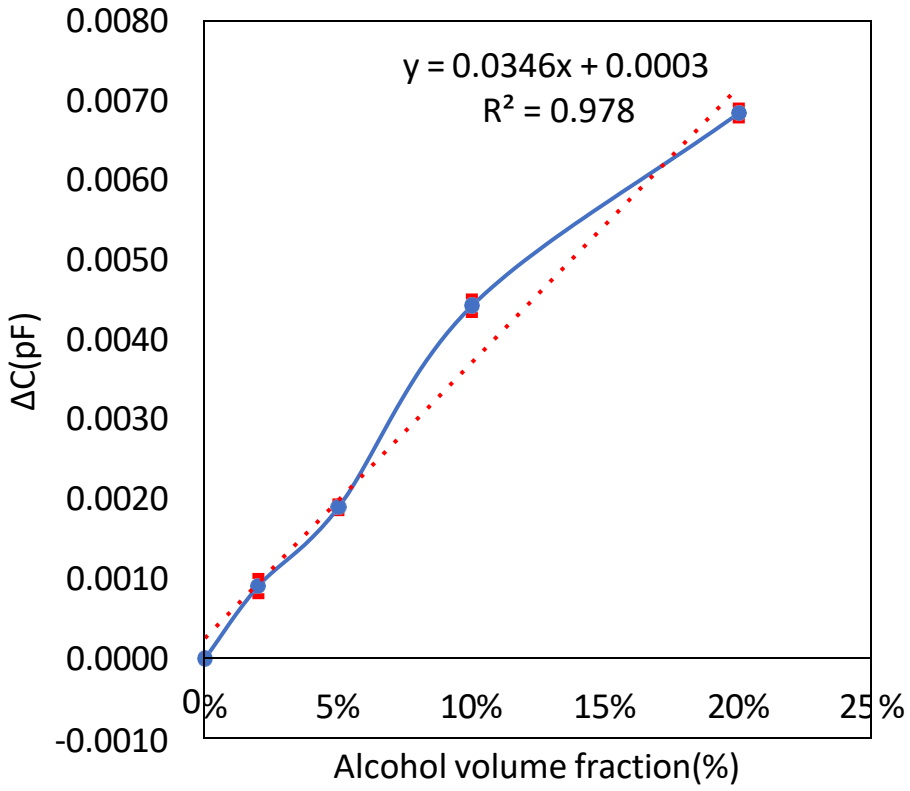

Figure 4.15 Capacitance change for different volume fraction of alcohol solutions.

4.5 DISCUSSION

For capacitive sensing for liquid detection, the liquid level could be measured by a single electrode CPC sensor at the container bottom. In our tests, if the container was made of non-conductive materials, the ΔC can be determined by the horizontal and vertical area that was covered with liquid. Generally, the ΔC was proportional to the area increase. However, the ΔC on the vertical direction was more predictable than that on horizontal

direction since the side area change was constant when volume of added water was fixed. The sensitivity of our sensor on liquid level detection was programmable because the slope varied based on the diameter of the container. Therefore, the container was able to be designed to the shape that fitted the required resolution and volume.

The liquid detection in conductive containers were also modeled and tested in practice. The sensitivity of our sensor was dampened by metal container. Since the ΔC was in femtofarad range, even the small disturbance of the test environment, the sensor, and objects would affect ΔC. To improve the accuracy and the stability of the measurement, the differential configuration and a well confined test stage were used.

The other applications such as liquid content differentiation and flow rate were conducted. The results proved that our sensor as well as the configuration were able to measure the ΔC which gave us the information for each specific task.

4.6 APPLICATIONS

The differential measurement was applied in a liquid level sensing system prototype which consisted of three parts, tubing with LED indicator, reservoir with LED graduation indicator, and as the reference tubing and reservoir. The system was designed to indicate when liquid passes through a tube with a green LED turning on during the flow. As reservoir filled from tube outlet, the LED graduation lights turned on with respect to the deposited water volume.

To construct two differential measurements in one system, 4 CPC capacitive sensors were arranged to construct two pairs of measurements; one was for flow in the tube

and the other was for the liquid level in the reservoir. The distance between the sensors and the tube and the reservoir was 1mm. A funnel was used to supply the liquid into the tube. A microprocessor was connected to FDC1004 to collect the capacitance data and control LEDs. Fig 4.16a showed the system setup. The demonstration test was conducted by the following steps: (1). 30mL of water was supplied into the funnel. (2) As water passed through the tube, the green LED indicator was turned on to show the water flow. (3) Water was supplied to the beaker from the outlet of the tube. (4) As the beaker was gradually filled with water, the LED was turned on. As water level increased, the LED strip sequentially turned on with respect to the level.

The data of the tubing and the reservoir of the entire procedure was recorded. Besides the water, we also tried to record the data for empty and carbonated water which gave us more insights of the system capability.

Fig 4.16 b,c and d depicted the results of the three test sets. The empty case showed that the capacitance value of the two pairs of differential measurements were steady with low noise. In the test of water, reservoir started to capture the ΔC by a few second delay in comparison to the tube. As more water was supplied to the funnel, the capacitance on the beaker accumulated while the ΔC of tube kept at around 200fF. As for the carbonated water, the high concentration of bubbles created spikes in the capacitance signal. The tube indicator was able to be turned on by the flowing carbonated water and the capacitance value of the reservoir still accumulated. However, the capacitance change was greater than pure water. The carbon dioxide gas bubbles showed the spikes of ΔC.

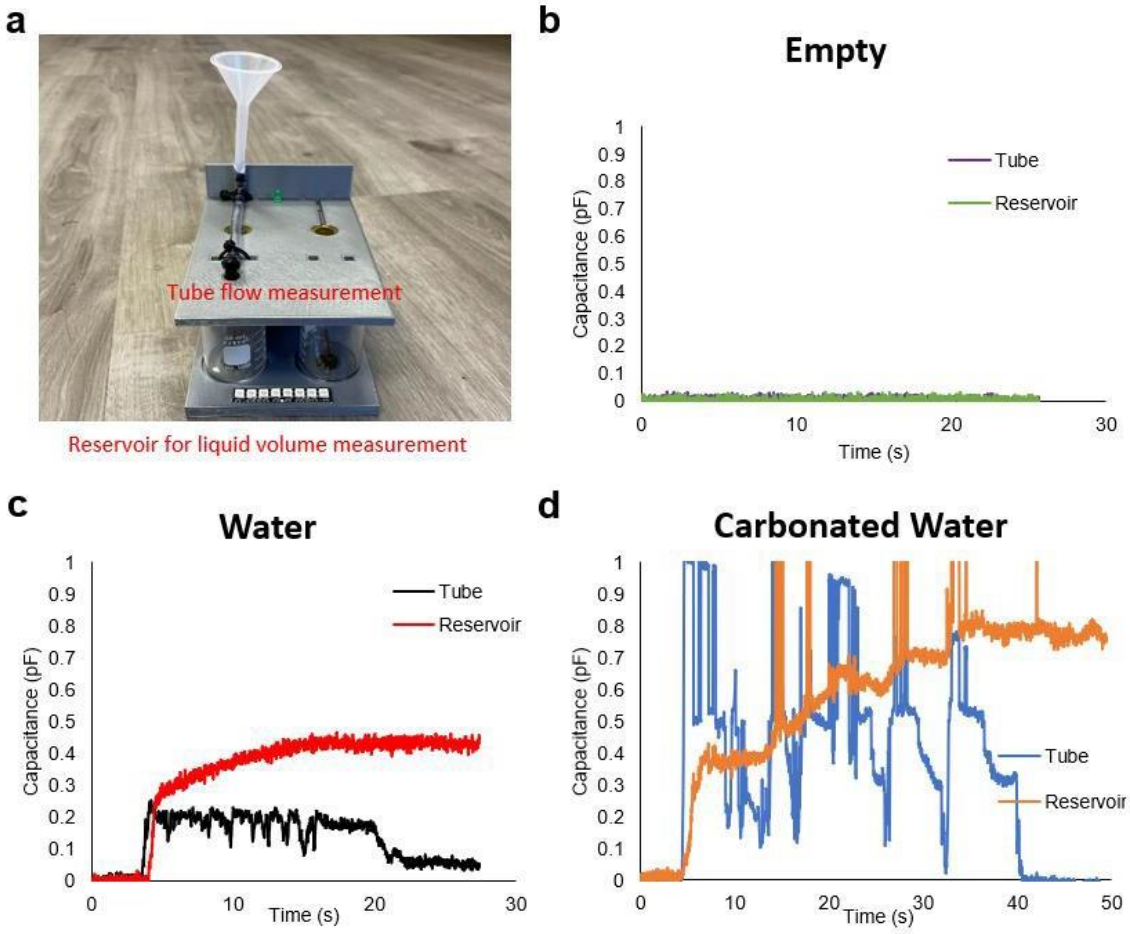

Figure 4.16 (a) Experiment setup for the application (b) Capacitance change if no water was supplied to the test setup. (c) Capacitance result of water as the test object to be added into the system. (d) Carbonated water test result

4.7 CONCLUSION

The self-capacitive single electrode sensor made of carbon nanotube composite (CPC) was demonstrated to detect the liquid level and volume in a dynamic range of hundreds of millimeters since the supplied liquid worked as the second electrode for ΔC. For non-conductive containers, the relationship between the ΔC and the container

dimension was studied to understand how to design the container to fulfill the diverse demands. Based on simulation and experiment results, high aspect ratio form factor had the better sensitivity for liquid volume measurement. In order to obtain a higher resolution of liquid level, a wider diameter was preferred. In comparison to single-ended configuration, the differential configuration consisting of two single electrode sensors was investigated which showed the better performance in terms of a signal to noise ratio. The liquid level detection of conductive containers was studied through differential measurement. The experimental result showed a stable and predictable capacitance change ΔC at each test level. The sensitivity of liquid volume and level for non-conductive containers was described in the following Table. 4.1and plotted in Fig 4.17 in which our sensor was compared to other capacitive liquid detection sensors. In terms of the resolution and detection ranges, the presented sensors showed the highest detection range per sensor without compromising the sensitivity. With the differential configuration and the measure circuit, the resolution was 0.2mm and the dynamic range was 100 mm/sensor. The presented single electrode CPC sensor showed the potential for non-contact liquid level sensing in various applications.

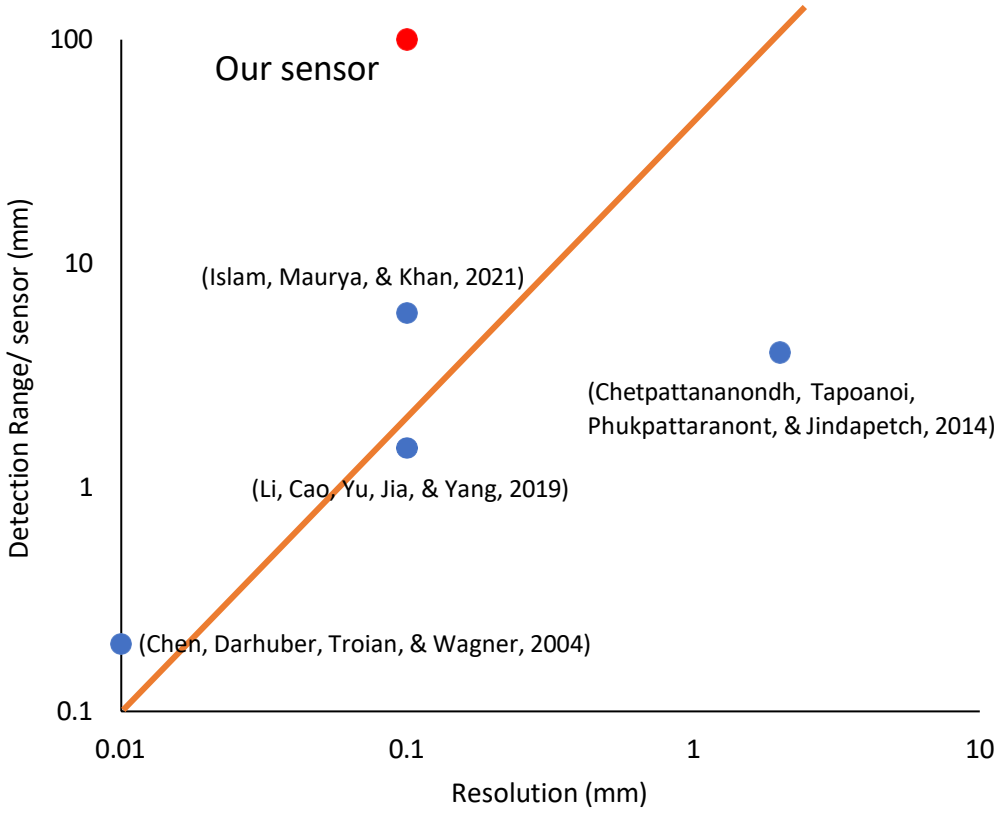

Figure 4.17 Comparison of the resolution and detection range of the presented capacitive sensor in comparison to other capacitive sensors.

Table 4.1 Comparison of the performance of the capacitive sensors used in liquid level detection.

Table 4.1

Ref	Electrode width	Electrode spacing	Number of electrodes	Placement	Resolution	Dynamic range/sensor	Sensitivity
[106]	2 mm	1 mm	7	Lateral	0.1 mm	<6 mm	40fF/mm
[107]	2 mm	2 mm	75	Lateral	2 mm	<4 mm	70pF/mm
[109]	0.1 mm	0.06 mm	2	Bottom	0.01 mm	<0.2 mm	30fF/μm
[112]	10 mm	6 mm	2	Bottom	0.1 mm	<1.5 mm	450fF/mm
This paper	**5 mm**	**x**	**1**	**Bottom**	**0.1mm**	**<100 mm**	**2fF/mm**

Chapter 5. GESTURE RECOGNITION USING A CPC CAPACITIVE SENSOR

5.1 INTRODUCTION

With the recent advancement of artificial intelligence and industrial 5.0, the human-machine interface (HMI) is under rapid development. In the implementation of human-machine interface (HMI), various sensors play a crucial role in detecting human behavior and cognitive response. Sensors collect foundational information to enable efficient communication, process control, and safety assurance. An intelligent system can use sensors to recognize human instructions, which can be conveyed through voice, gestures, and body movements. The detection of industrial processes and environmental change is a crucial process to warrant safety and health. Among the various sensing mechanisms, the capacitance sensing is unique as it can detect both proximity and contacts at a fraction of cost and power consumption to camera-based or radar-based technologies.

This chapter presents a capacitive sensor composed of a nanostructured electrode array. A capacitive electrode is composed of high aspect-ratio cellulose fibers embedded with multiwalled carbon nanotubes. The electrode array enlarges the capacitance with a small form factor. The highly sensitive sensors are fabricated as a smart pad, which is utilized for gesture recognition.

5.2 EXPERIMENT METHOD

5.2.1 *Fabrication of fibrous electrodes*

Fibrous electrodes were fabricated by controlled water-printing and stretching [69]. Silver paste (MG Chemicals, USA) was applied and cured to both ends of a strip made of carbon nanotube paper composite strip. Using a 0.7 mm-diameter capillary pen, water was printed three times to fully absorb water at a fracture location. A pair of fibrous electrodes was produced by stretching the strip. The fabricated widths of fibrous electrodes were 10 mm. A silver-coated-polyester film electrode is a rectangular electrode as shown Fig 5.1.

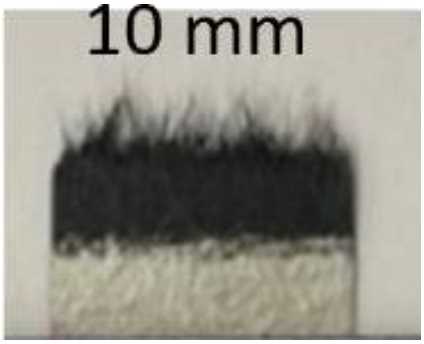

Figure 5.1 10mm width silver-coated-CPC electrode

5.2.2 *Fabrication of the smart plate*

A four-sensor array smart pad was designed and fabricated with 3D printer (Fig 5.2). Considering the flexibility of employing the sensor system in a larger scale of applications, the smart pad can be assembled in an array format. In one pad, the four sensors were connected to a capacitance-to-digital chip (FDC1004, Texas Instrument). The measurement data were transferred to the microcontroller (ATmega328PU) at a sampling frequency of 18Hz.

Figure 5.2 Design of a smart pad. Four sensors are radially arranged on a 3D printed plate. 10 mm-wide single fibrous electrodes were used for monitoring human behavior and an object. Each plate can be assembled to form a sensor array.

The detection range of hand for each sensor was similar and about 300mm on a electrically non-conductive table. If the pad was placed on a conductive table or on the floor, the detectable range was weakened. To demonstrate the usability of the smart pad, the tests were conducted on a wood table.

5.3 Experimental Result and Discussion

Using the sensors, we could only obtain the signals from the sensing spots. To have a better visualization, a simulation was attempted in COMSOL showed in Fig 5.3. In the simulation, an identical dimension of the pad was generated, and the sensors were located in the same position on the pad. The object was set to be a series of specific distances (1,

2, 3, 4, 5, and 6 mm) above the pad to perform as the human hand. Then the object was set to the specific height and sweep from the left bottom corner to right bottom corner in 10 steps and repeat the same sweep from bottom to top in 10 steps. The result of the capacitance change for top left sensor was plotted in 2D and 3D formats (Fig 5.3). Since each sensor was behaving in a similar manner when they were put in a relatively far distance, the capacitance's distribution on the board was the superposition of distribution of all four sensors. Therefore, to reproduce the visualization of the 3D capacitance distribution, the equation of the capacitance value for each spot in the map should be generated. The Gaussian equation was chosen to fit the surface (Fig 5.2b).

$$f(x) = a \cdot \exp\left(-\left(\frac{(x-b)^2}{2c^2} + \frac{(y-d)^2}{2e^2}\right)\right) \tag{5.1}$$

In the figure, the blue dots were the result values from simulation. The surface was plotted through Gaussian equation which offered a decent match. In the equation, a was the measurement value from sensor, b and d were the dimensions of each spot in the map, and c was the coefficient according to a. Therefore, with the equation, the spots without sensor embedded then could be interpolated, which gave us the opportunity to visualize the capacitance distribution. When signals of sensors were transferred to computer, the contour map for each sensor was calculated, then four contour plots were added up together to produce the final visualized real-time 3D contour map.

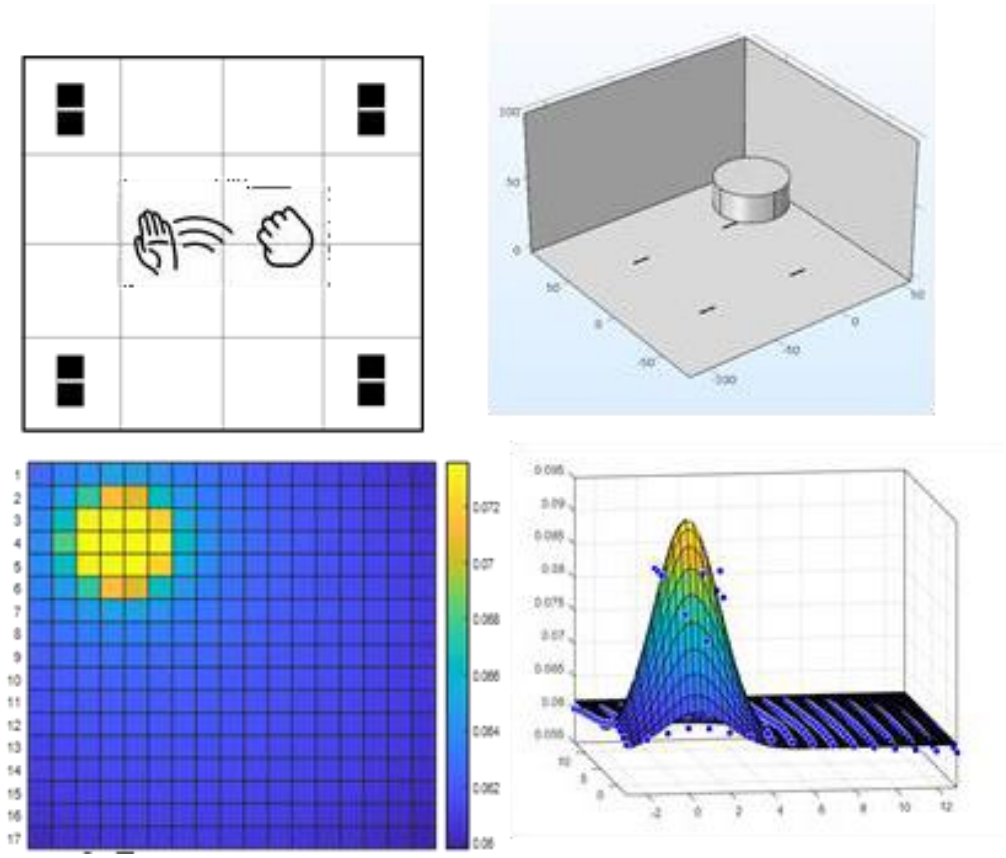

Figure 5.3 ΔC model for four sensors based on the numerical model

A few tests were conducted to visualize the sensing performance of the smart pad through the real-time 3D contour map. The pad was placed on a table for calibration first. After one second of the calibration, the baseline values of all the four sensors were recorded. When a foot with shoe on steps on the board, the pressurized area covered 2 sensors and caused the capacitance change on the covered sensors (Fig 5.4). Through the contour map, the graph showed the profile of the capacitance value increase. After removal of the foot, the capacitance value would return to the original baseline and the graph profile returned to the origin accordingly. A test of liquid filling with a glass beaker was also conducted

and shown in Fig 5.4. One glass cup was placed on one of the sensors and with the addition of water. The real-time graph was plotted based on the capacitance change.

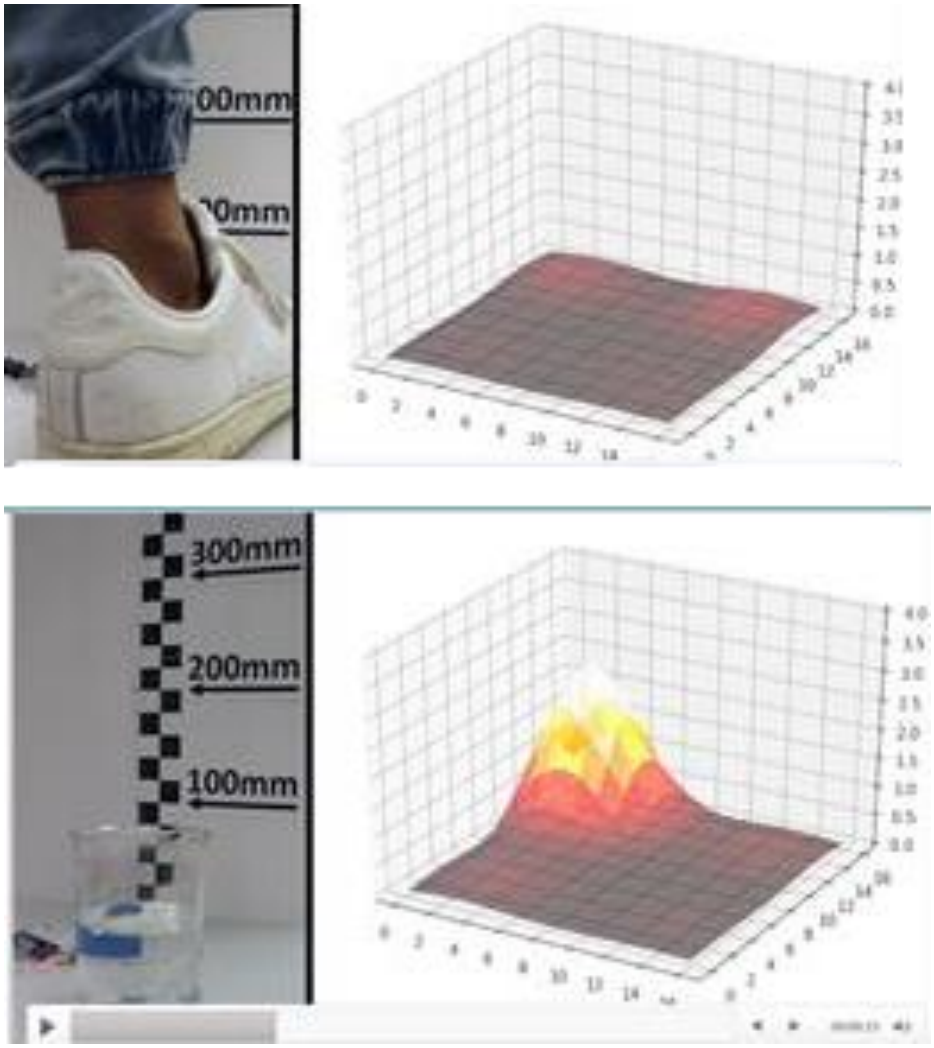

Figure 5.4 Contour map for step test and liquid test on the smart pad.

With the deployment of the artificial intelligence algorithm, this intelligent sensor array system could recognize the instruction from the operator.

Firstly, a machine learning model needed to be trained with the time series data from the sensors. The sampling rate and the time window for each gesture or motion had

to be determined before the data collection. In our experiment, the sampling rate was set to 18Hz and time window for each motion was 3 second which was an appropriate for a human to perform a wave or a grab. Therefore, the function of the ML model was to classify the motion based on the input time series data.

The data set preparation consisted of three parts. The motion of waving hand from left of the pad to right and grabbing should be performed above the pad and repeat 30 times. And the control without hand intervention was also needed as the reference signals. To have an initial sense of the data for the motion measured by the sensors' array, the data for each motion within a time window were plotted in Fig 5.5. Without any motion played beyond the pad, the capacitance values measured by sensors were almost flat with noise level of 40fF. The signals of two motions had the larger magnitude change in terms of capacitance value. Due to the different pattern of the motions, the order of the occurrence of peak for each sensor was distinguishable.

After the data collection, the entire data set was put into a machine learning model package, Sktime whose expertise was the classification of time series data. When the training was complete, the model was saved to a file which could be applied to the real-time classification of hand motion. The performance of the classifier could recognize human gesture with 95% accuracy in a real-time hand motion.

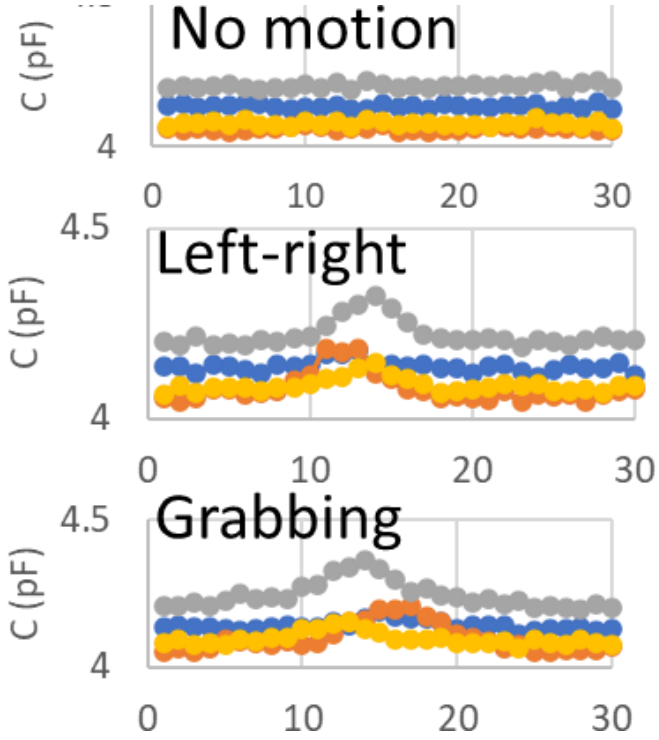

Figure 5.5 Time profile of gesture recognition test of a smart plate for different motion.

5.4 CONCLUSION

Ultrasensitive capacitive sensors composed of nanostructured fibrous electrodes were demonstrated for human-machine interface. A smart pad could be constructed to recognize human behavior, detect object, and gait. The ultrasensitive capacitive sensor facilitates the delicate detection of human behavior, environmental change, manufacturing process, and safety control.

Chapter 6. CONCLUSION AND FUTURE RESEARCH PLAN

6.1 SUMMARY OF CONTRIBUTION

In summary, the capacitive sensing mechanism of an auxetic CPC composite was presented and studied for humidity and liquid level detection.

When a water-printed CPC composite was stretched, the auxetic behavior produced the radial structures of cellulose fibers embedded with MWCNTs. The high aspect ratio fibers of fractured CPC generated crossing junctions at the crack of the water-printed region. Water molecules introduced on the surface of the crossing radial structure enlarged the capacitance change among the high aspect ratio electrodes, resulting in the extreme change of capacitance. According to our further analysis, the capacitive sensitivity to humidity was originated from the crossing molecular junctions of conductive fibers that trapped water molecules. Due to the molecular junctions, a large change of capacitance could be obtained without a humidity absorption pad. An empirical equation between capacitance and RH was obtained by calibration with a reference humidity sensor. The normalized capacitance change ($\Delta C/C$) for a CPC humid sensor was 0.225 in the relative humidity ranging 40~80 %. The CPC-capacitive sensor could be used for sweating measurements on the hand. The auxetically produced capacitive sensing platform can facilitate a wearable sensor measuring humidity and sweat.

The self-capacitive single-electrode sensor made of carbon nanotube composite (CPC) was demonstrated to detect the liquid level and volume. The sensing mechanism was studied by numerical and experimental methods. To improve the resolution and accuracy, the differential measurement was studied and tested for single electrode

capacitive CPC sensor. For non-conductive containers, the relationship between the ΔC and the container dimension was studied to understand how to design the container to fulfill the diverse demands. The liquid level detection of conductive containers was studied through differential measurement. The sensitivity of liquid volume and level for non-conductive containers was obtained and compared with other capacitive sensors. In terms of the resolution and dynamic ranges, the presented sensors showed the highest dynamic range per sensor without compromising the sensitivity. With the differential configuration and the measure circuit, the resolution was 0.2mm and the dynamic range was 100 mm/sensor.

The smart pad was constructed with an array of fractured CPC sensors to recognize the human motion, gesture, object, and gait. With the further development of the sensing system and machine learning algorithm, the presented ultrasensitive capacitive sensors can be potentially applied to various non-contact detections, such as vending machine, process automation, gesture recognition, and other human machine interfaces.

6.2 FUTURE PLAN

The capacitive CPC sensor was studied and proven to be sensitive to liquid in a non-contact manner. The advantages of paper composite such as cost effective and flexibility provided the potential applications to various human machine interfaces.

Based on CPC's sensitivity to rapid humid change, a new generation of humid sensing system could be considered for factory automation. A novel non-contact liquid detection system that can measure both the level and volume could be designed based on the industry demand. By employing the differential measurement, a high accuracy liquid detection system could be considered to conduct sophisticated tasks.

Acknowledgement

The authors acknowledge the support from the Advanced Manufacturing Program of National Science Foundation (No. 1927623). ZQ, ABD, and JC acknowledge the partial support from IP group and Somalytics. The study related to sweat monitoring was approved by the institutional review board (IRB) at the University of Washington (IRB ID: STUDY00010741).

References

1. Bao, G.J., et al., *Academic Review and Perspectives on Robotic Exoskeletons.* Ieee Transactions on Neural Systems and Rehabilitation Engineering, 2019. **27**(11): p. 2294-2304.
2. Wang, H.W., et al., *Effectiveness of interventions to improve hand motor function in individuals with moderate to severe stroke: a systematic review protocol.* Bmj Open, 2019. **9**(9).
3. Kristensen, S.E., et al., *Robot-assisted surgery in gynecological oncology: current status and controversies on patient benefits, cost and surgeon conditions - a systematic review.* Acta Obstetricia Et Gynecologica Scandinavica, 2017. **96**(3): p. 274-285.
4. Iqbal, J., Z.H. Khan, and A. Khalid, *Prospects of robotics in food industry.* Food Science and Technology, 2017. **37**(2): p. 159-165.
5. Xu, J.J., et al., *A Review on Significant Technologies Related to the Robot-Guided Intelligent Bolt Assembly Under Complex or Uncertain Working Conditions.* Ieee Access, 2019. **7**: p. 136752-136776.
6. Zhou, Z.D., et al., *Disassembly sequence planning: Recent developments and future trends.* Proceedings of the Institution of Mechanical Engineers Part B-Journal of Engineering Manufacture, 2019. **233**(5): p. 1450-1471.
7. Wang, L., et al., *Overview of Human-Robot Collaboration in Manufacturing*. 2020. 15-58.
8. Kapuscinski, T., et al., *Recognition of Hand Gestures Observed by Depth Cameras.* International Journal of Advanced Robotic Systems, 2015. **12**.
9. Katsuki, Y., Y. Yamakawa, and M. Ishikawa. *High-speed human/robot hand interaction system*. in *Proceedings of the Tenth Annual ACM/IEEE International Conference on Human-Robot Interaction Extended Abstracts*. 2015.
10. Oudah, M., A. Al-Naji, and J. Chahl, *Hand Gesture Recognition Based on Computer Vision: A Review of Techniques.* Journal of Imaging, 2020. **6**(8).
11. Paredes, J.D.A., et al. *A reliability assessment software using Kinect to complement the clinical evaluation of Parkinson's disease*. in *2015 37th Annual International*

Conference of the IEEE Engineering in Medicine and Biology Society (EMBC). 2015.

12. Patel, S., et al., *A review of wearable sensors and systems with application in rehabilitation.* Journal of Neuroengineering and Rehabilitation, 2012. **9**.
13. Rodgers, M.M., V.M. Pai, and R.S. Conroy, *Recent Advances in Wearable Sensors for Health Monitoring.* Ieee Sensors Journal, 2015. **15**(6): p. 3119-3126.
14. Mathew, M., et al., *Flexible and wearable electrochemical biosensors based on two-dimensional materials: Recent developments.* Analytical and Bioanalytical Chemistry, 2021. **413**(3): p. 727-762.
15. Yousef, H., M. Boukallel, and K. Althoefer, *Tactile sensing for dexterous in-hand manipulation in robotics-A review.* Sensors and Actuators a-Physical, 2011. **167**(2): p. 171-187.
16. Hussain, I., et al., *Vibrotactile Haptic Feedback for Intuitive Control of Robotic Extra Fingers*. 2015.
17. Heinz, E.A., et al. *Using Wearable Sensors for Real-Time Recognition Tasks in Games of Martial Arts - An Initial Experiment*. in *2006 IEEE Symposium on Computational Intelligence and Games*. 2006.
18. Cheng, Y., et al., *A Stretchable and Highly Sensitive Graphene-Based Fiber for Sensing Tensile Strain, Bending, and Torsion.* Advanced Materials, 2015. **27**(45): p. 7365-+.
19. Trung, T.Q., et al., *An All-Elastomeric Transparent and Stretchable Temperature Sensor for Body-Attachable Wearable Electronics.* Advanced Materials, 2016. **28**(3): p. 502-+.
20. Lee, H., et al., *Wearable/disposable sweat-based glucose monitoring device with multistage transdermal drug delivery module.* Science Advances, 2017. **3**(3).
21. Phan, D., et al. *Smartwatch: Performance evaluation for long-term heart rate monitoring*. in *2015 International Symposium on Bioelectronics and Bioinformatics (ISBB)*. 2015.
22. Edwards, J., *Wireless Sensors Relay Medical Insight to Patients and Caregivers.* Ieee Signal Processing Magazine, 2012. **29**(3): p. 8-12.

23. Malhi, K., et al., *A Zigbee-Based Wearable Physiological Parameters Monitoring System.* Ieee Sensors Journal, 2012. **12**(3): p. 423-430.
24. Salvo, P., et al., *A Wearable Sensor for Measuring Sweat Rate.* Ieee Sensors Journal, 2010. **10**(10): p. 1557-1558.
25. Chen, B.R., et al., *A Web-Based System for Home Monitoring of Patients With Parkinson's Disease Using Wearable Sensors.* Ieee Transactions on Biomedical Engineering, 2011. **58**(3): p. 831-836.
26. Allet, L., et al., *Wearable Systems for Monitoring Mobility-Related Activities in Chronic Disease: A Systematic Review.* Sensors, 2010. **10**(10): p. 9026-9052.
27. Katzmarzyk, P.T. and I. Janssen, *The economic costs associated with physical inactivity and obesity in Canada: An update.* Canadian Journal of Applied Physiology-Revue Canadienne De Physiologie Appliquee, 2004. **29**(1): p. 90-115.
28. Pan, D., et al., *A Mobile Cloud-Based Parkinson's Disease Assessment System for Home-Based Monitoring.* Jmir Mhealth and Uhealth, 2015. **3**(1).
29. Kiliboz, N.C. and U. Gudukbay, *A hand gesture recognition technique for human-computer interaction.* Journal of Visual Communication and Image Representation, 2015. **28**: p. 97-104.
30. Bozomitu, R.G., et al., *Development of an Eye Tracking-Based Human-Computer Interface for Real-Time Applications.* Sensors, 2019. **19**(16).
31. Koshy, M.M. and S. Karthikeyan, *EOG Technology for Communication Between Deaf and Dumb People Using Eye Blink Sensor.* Research Journal of Pharmaceutical Biological and Chemical Sciences, 2017. **8**(3): p. 2003-2014.
32. Kawato, S. and N. Tetsutani, *Detection and tracking of eyes for gaze-camera control.* Image and Vision Computing, 2004. **22**(12): p. 1031-1038.
33. Cheung, Y.M. and Q.M. Peng, *Eye Gaze Tracking With a Web Camera in a Desktop Environment.* Ieee Transactions on Human-Machine Systems, 2015. **45**(4): p. 419-430.
34. Peternel, L. and J. Babič, *Learning of compliant human–robot interaction using full-body haptic interface.* Advanced Robotics, 2013. **27**(13): p. 1003-1012.

35. Agravante, D.J., et al. *Collaborative human-humanoid carrying using vision and haptic sensing*. in *2014 IEEE International Conference on Robotics and Automation (ICRA)*. 2014.
36. Peternel, L., et al., *Robot adaptation to human physical fatigue in human-robot co-manipulation.* Autonomous Robots, 2018. **42**(5): p. 1011-1021.
37. Wu, X.Y., et al., *Surveillance Robot Utilizing Video and Audio Information.* Journal of Intelligent & Robotic Systems, 2009. **55**(4-5): p. 403-421.
38. Cao, J.T., et al., *THE VISUAL-AUDIO INTEGRATED RECOGNITION METHOD FOR USER AUTHENTICATION SYSTEM OF PARTNER ROBOTS.* International Journal of Humanoid Robotics, 2011. **8**(4): p. 691-705.
39. Asokan, A., A. Pothen, and R.K. Vijayaraj, *ARMatron — A wearable gesture recognition glove: For control of robotic devices in disaster management and human Rehabilitation*. 2016. 1-5.
40. Assad, C., et al. *Live demonstration: BioSleeve, a wearable hands-free gesture control interface*. in *2016 IEEE SENSORS*. 2016.
41. Yang, C.C. and Y.L. Hsu, *A Review of Accelerometry-Based Wearable Motion Detectors for Physical Activity Monitoring.* Sensors, 2010. **10**(8): p. 7772-7788.
42. Gopinath, V. and K. Johansen, *Understanding situational and mode awareness for safe human-robot collaboration: case studies on assembly applications.* Production Engineering-Research and Development, 2019. **13**(1): p. 1-9.
43. El Zaatari, S., et al., *Cobot programming for collaborative industrial tasks: An overview.* Robotics and Autonomous Systems, 2019. **116**: p. 162-180.
44. Bi, L.Z., A.G. Feleke, and C.T. Guan, *A review on EMG-based motor intention prediction of continuous human upper limb motion for human-robot collaboration.* Biomedical Signal Processing and Control, 2019. **51**: p. 113-127.
45. Nardelli, M.B., et al., *Mechanical properties, defects and electronic behavior of carbon nanotubes.* Carbon, 2000. **38**(11-12): p. 1703-1711.
46. Dong, Z.J., et al., *A review of aligned carbon nanotube arrays and carbon/carbon composites: fabrication, thermal conduction properties and applications in thermal management.* New Carbon Materials, 2021. **36**(5): p. 873-892.

47. Thostenson, E.T., et al., *Electrical anisotropy in multiscale nanotube/fiber hybrid composites.* Applied Physics Letters, 2009. **95**(7).
48. Qi, H.S., et al., *Cellulose fibres with carbon nanotube networks for water sensing.* Journal of Materials Chemistry A, 2014. **2**(15): p. 5541-5547.
49. Park, M., H. Kim, and J.P. Youngblood, *Strain-dependent electrical resistance of multi-walled carbon nanotube/polymer composite films.* Nanotechnology, 2008. **19**(5).
50. Ahmed, S., M.P.N. Bui, and A. Abbas, *Paper-based chemical and biological sensors: Engineering aspects.* Biosensors & Bioelectronics, 2016. **77**: p. 249-263.
51. Wang, Z., et al., *Progress in Auxetic Mechanical Metamaterials: Structures, Characteristics, Manufacturing Methods, and Applications.* Advanced Engineering Materials, 2020. **22**(10): p. 2000312.
52. Wu, W.W., et al., *Mechanical design and multifunctional applications of chiral mechanical metamaterials: A review.* Materials & Design, 2019. **180**.
53. Almgren, R.F., *AN ISOTROPIC 3-DIMENSIONAL STRUCTURE WITH POISSON RATIO=-1.* Journal of Elasticity, 1985. **15**(4): p. 427-430.
54. Grima, J.N. and K.E. Evans, *Auxetic behavior from rotating squares.* Journal of Materials Science Letters, 2000. **19**(17): p. 1563-1565.
55. Zega, V., et al., *Design, fabrication and experimental validation of a MEMS periodic auxetic structure.* Smart Materials and Structures, 2019. **28**(9): p. 095011.
56. Evans, K.E. and A. Alderson, *Auxetic materials: Functional materials and structures from lateral thinking!* Advanced Materials, 2000. **12**(9): p. 617-+.
57. Li, D.C., et al., *A review of modelling and analysis of morphing wings.* Progress in Aerospace Sciences, 2018. **100**: p. 46-62.
58. Trung, T.Q. and N.E. Lee, *Flexible and Stretchable Physical Sensor Integrated Platforms for Wearable Human-Activity Monitoring and Personal Healthcare.* Advanced Materials, 2016. **28**(22): p. 4338-4372.
59. Shintake, J., T. Nagai, and K. Ogishima, *Sensitivity Improvement of Highly Stretchable Capacitive Strain Sensors by Hierarchical Auxetic Structures.* Frontiers in Robotics and AI, 2019. **6**.

60. Peng, R., et al., *Two-dimensional materials with intrinsic auxeticity: progress and perspectives.* Nanoscale, 2019. **11**(24): p. 11413-11428.
61. Stenberg, N. and C. Fellers, *Out-of-plane Poisson's ratios of paper and paperboard.* Nordic Pulp & Paper Research Journal, 2002. **17**(4): p. 387-394.
62. Thirlwell, B.E. and L.R.G. Treloar, *Non-Woven Fabrics. Part VI: Dimensional and Mechanical Anisotropy.* Textile Research Journal, 1965. **35**(9): p. 827-835.
63. Dirrenberger, J., et al., *Homogenization of periodic auxetic materials.* Procedia Engineering, 2011. **10**: p. 1847-1852.
64. Korner, C. and Y. Liebold-Ribeiro, *A systematic approach to identify cellular auxetic materials.* Smart Materials and Structures, 2015. **24**(2).
65. Domaschke, S., et al., *Random auxetics from buckling fibre networks.* Nature Communications, 2019. **10**.
66. Amjadi, M., et al., *Highly Stretchable and Sensitive Strain Sensor Based on Silver Nanowire-Elastomer Nanocomposite.* Acs Nano, 2014. **8**(5): p. 5154-5163.
67. Park, J.J., et al., *Highly Stretchable and Wearable Graphene Strain Sensors with Controllable Sensitivity for Human Motion Monitoring.* ACS Applied Materials & Interfaces, 2015. **7**(11): p. 6317-6324.
68. Goodman, S.M., et al., *Scalable manufacturing of fibrous nanocomposites for multifunctional liquid sensing.* Nano Today, 2021. **40**: p. 101270.
69. Zhang, J.Y., et al., *Electromechanical coupling of isotropic fibrous networks with tailored auxetic behavior induced by water-printing under tension.* Journal of Materials Chemistry C, 2021. **9**(13): p. 4544-4553.
70. Zhang, J.-Y., et al., *Fracture-Induced Mechano-Electrical Sensitivities of Paper-Based Nanocomposites.* Advanced Materials Technologies, 2018. **3**(3): p. 1700266.
71. Dichiara, A.B., et al., *Smart papers comprising carbon nanotubes and cellulose microfibers for multifunctional sensing applications.* Journal of Materials Chemistry A, 2017. **5**(38): p. 20161-20169.
72. Goodman, Sheila M., N. Ferguson, and A.B. Dichiara, *Lignin-assisted double acoustic irradiation for concentrated aqueous dispersions of carbon nanotubes.* RSC Advances, 2017. **7**(9): p. 5488-5496.

73. Qi, H.S., E. Mader, and J.W. Liu, *Unique water sensors based on carbon nanotube-cellulose composites.* Sensors and Actuators B-Chemical, 2013. **185**: p. 225-230.
74. Zampetti, E., et al., *Design and optimization of an ultra thin flexible capacitive humidity sensor.* Sensors and Actuators B: Chemical, 2009. **143**(1): p. 302-307.
75. Kim, J., et al., *Capacitive Humidity Sensor Based on Carbon Black/Polyimide Composites.* Sensors, 2021. **21**(6): p. 1974.
76. Gu, L., Q.-A. Huang, and M. Qin, *A novel capacitive-type humidity sensor using CMOS fabrication technology.* Sensors and Actuators B: Chemical, 2004. **99**(2): p. 491-498.
77. Boudaden, J., et al., *Polyimide-Based Capacitive Humidity Sensor.* Sensors, 2018. **18**(5): p. 1516.
78. Liu, J., et al., *In situ growth of continuous thin metal–organic framework film for capacitive humidity sensing.* Journal of Materials Chemistry, 2011. **21**(11): p. 3775-3778.
79. Chappanda, K.N., et al., *Trianglamine hydrochloride crystals for a highly sensitive and selective humidity sensor.* Sensors and Actuators B: Chemical, 2019. **294**: p. 40-47.
80. Steele, J.J., G.A. Fitzpatrick, and M.J. Brett, *Capacitive Humidity Sensors With High Sensitivity and Subsecond Response Times.* IEEE Sensors Journal, 2007. **7**(6): p. 955-956.
81. Rauf, S., et al., *Highly Selective Metal–Organic Framework Textile Humidity Sensor.* ACS Applied Materials & Interfaces, 2020. **12**(26): p. 29999-30006.
82. Han, K.I., et al., *Compliment Graphene Oxide Coating on Silk Fiber Surface via Electrostatic Force for Capacitive Humidity Sensor Applications.* Sensors, 2017. **17**(2): p. 407.
83. Hernández-Rivera, D., et al., *A Capacitive Humidity Sensor Based on an Electrospun PVDF/Graphene Membrane.* Sensors, 2017. **17**(5): p. 1009.
84. Altenberend, U., et al., *Towards fully printed capacitive gas sensors on flexible PET substrates based on Ag interdigitated transducers with increased stability.* Sensors and Actuators B: Chemical, 2013. **187**: p. 280-287.

85. Gaspar, C., et al., *Paper as Active Layer in Inkjet-Printed Capacitive Humidity Sensors.* Sensors, 2017. **17**(7): p. 1464.
86. Li, X.Y., et al., *High-sensitive humidity sensor based on graphene oxide with evenly dispersed multiwalled carbon nanotubes.* Materials Chemistry and Physics, 2018. **207**: p. 135-140.
87. Boutros, S. and A.A. Hanna, *Dielectric properties of moist cellulose.* Journal of Polymer Science: Polymer Chemistry Edition, 1978. **16**(1): p. 89-94.
88. Murphy, E.J., *Electrical conduction in textiles II Alternating current conduction in cotton and silk.* Journal of Physical Chemistry, 1929. **33**(1): p. 200-215.
89. Wang, Y. and M.N. Afsar, *Measurement of complex permittivity of liquid dielectrics.* Microwave and Optical Technology Letters, 2002. **34**(4): p. 240-243.
90. Liu, C.J. and F. Tong, *An SIW Resonator Sensor for Liquid Permittivity Measurements at C Band.* Ieee Microwave and Wireless Components Letters, 2015. **25**(11): p. 751-753.
91. Chiu, T., *Dielectric constant measurement technique for a dielectric strip using a rectangular waveguide.* Ieee Transactions on Instrumentation and Measurement, 2003. **52**(5): p. 1501-1508.
92. Praveen, K., et al., *A novel technique towards deployment of hydrostatic pressure based level sensor in nuclear fuel reprocessing facility.* Review of Scientific Instruments, 2016. **87**(2).
93. Antonio-Lopez, J.E., D.A. May-Arrioja, and P. LiKamWa, *Fiber-Optic Liquid Level Sensor.* Ieee Photonics Technology Letters, 2011. **23**(23): p. 1826-1828.
94. Hauptmann, P., N. Hoppe, and A. Puttmer, *Application of ultrasonic sensors in the process industry.* Measurement Science and Technology, 2002. **13**(8): p. R73-R83.
95. Loizou, K. and E. Koutroulis, *Water level sensing: State of the art review and performance evaluation of a low-cost measurement system.* Measurement, 2016. **89**: p. 204-214.
96. Toth, F.N., G.C.M. Meijer, and M. vanderLee, *A planar capacitive precision gauge for liquid-level and leakage detection.* Ieee Transactions on Instrumentation and Measurement, 1997. **46**(2): p. 644-646.

97. Rajamani, A.S., M. Divagar, and V.V.R. Sai, *Plastic fiber optic sensor for continuous liquid level monitoring.* Sensors and Actuators a-Physical, 2019. **296**: p. 192-199.
98. Puers, R., *CAPACITIVE SENSORS - WHEN AND HOW TO USE THEM.* Sensors and Actuators a-Physical, 1993. **37-8**: p. 93-105.
99. Ernst, A., et al., *A capacitive sensor for non-contact nanoliter droplet detection.* Sensors and Actuators a-Physical, 2009. **153**(1): p. 57-63.
100. Canbolat, H., *A Novel Level Measurement Technique Using Three Capacitive Sensors for Liquids.* Ieee Transactions on Instrumentation and Measurement, 2009. **58**(10): p. 3762-3768.
101. Hu, L.Z., K. Toyoda, and I. Ihara, *Dielectric properties of edible oils and fatty acids as a function of frequency, temperature, moisture and composition.* Journal of Food Engineering, 2008. **88**(2): p. 151-158.
102. Fendri, A., et al., *Measurement System for Lossy Capacitive Sensors: Application to Edible Oils Quality Assessment.* Sensors, 2019. **19**(19).
103. Dean, R.N., et al., *A Capacitive Fringing Field Sensor Design for Moisture Measurement Based on Printed Circuit Board Technology.* Ieee Transactions on Instrumentation and Measurement, 2012. **61**(4): p. 1105-1112.
104. McIntosh, R.B. and M.E. Casada, *Fringing field capacitance sensor for measuring the moisture content of agricultural commodities.* Ieee Sensors Journal, 2008. **8**(3-4): p. 240-247.
105. Ruth, S.R.A., et al., *Flexible Fringe Effect Capacitive Sensors with Simultaneous High-Performance Contact and Non-Contact Sensing Capabilities.* Small Structures, 2021. **2**(2).
106. Islam, T., O.P. Maurya, and A.U. Khan, *Design and Fabrication of Fringing Field Capacitive Sensor for Non-Contact Liquid Level Measurement.* Ieee Sensors Journal, 2021. **21**(21): p. 24812-24819.
107. Chetpattananondh, K., et al., *A self-calibration water level measurement using an interdigital capacitive sensor.* Sensors and Actuators a-Physical, 2014. **209**: p. 175-182.

108. Yang, Q., et al., *An inkjet-printed capacitive sensor for water level or quality monitoring: investigated theoretically and experimentally.* Journal of Materials Chemistry A, 2017. **5**(34): p. 17841-17847.
109. Chen, J.Z., et al., *Capacitive sensing of droplets for microfluidic devices based on thermocapillary actuation.* Lab on a Chip, 2004. **4**(5): p. 473-480.
110. Huang, Y., Z. Zhan, and N. Bowler, *Optimization of the coplanar interdigital capacitive sensor.* AIP Conference Proceedings, 2017. **1806**(1): p. 110017.
111. Mizuguchi, J., et al., *Fringing Field Capacitive Sensor for Measuring Soil Water Content: Design, Manufacture, and Testing.* Ieee Transactions on Instrumentation and Measurement, 2015. **64**(1): p. 212-220.
112. Li, N., et al., *High Sensitive Capacitive Sensing Method for Thickness Detection of the Water Film on an Insulation Surface.* Ieee Access, 2019. **7**: p. 96384-96391.
113. Li, X.B.B., et al., *Design principles for multicuhannel fringing electric field sensors.* Ieee Sensors Journal, 2006. **6**(2): p. 434-440.
114. Hu, X.H. and W.Q. Yang, *Planar capacitive sensors - designs and applications.* Sensor Review, 2010. **30**(1): p. 24-39.
115. El-Adawy, M., et al., *Numerical Simulation of the Electrical Double Layer Development: Physicochemical Model at the Solid and Dielectric Liquid Interface for Laminar Flow Electrification Phenomenon.* Ieee Transactions on Dielectrics and Electrical Insulation, 2011. **18**(5): p. 1463-1475.
116. Dutta, A., et al., *Study of a Noncontact Flow Transducer Using Semicylindrical Capacitive Sensor.* Ieee Transactions on Instrumentation and Measurement, 2021. **70**.
117. Bera, S.C. and H. Mandal, *A Flow Measurement Technique Using a Noncontact Capacitance-Type Orifice Transducer for a Conducting Liquid.* Ieee Transactions on Instrumentation and Measurement, 2012. **61**(9): p. 2553-2559.
118. Ji, H.F., et al., *Measurement of Gas-Liquid Two-Phase Flow in Micro-Pipes by a Capacitance Sensor.* Sensors, 2014. **14**(12): p. 22431-22446.
119. Tang, X.Y., et al., *New method for bubble/slug velocity measurement in small channels.* Review of Scientific Instruments, 2020. **91**(5).

120. Zhang, J.Y., et al., *Fracture-Induced Mechanoelectrical Sensitivities of Paper-Based Nanocomposites.* Advanced Materials Technologies, 2018. **3**(3).